THE SOLID PARTICLE EROSION OF TUNGSTEN CARBIDE IN SILICON CARBIDE SLURRY

MICHAEL JOHN SANDSTROM

Department of Mechanical Engineering

University of Utah

December 2003

THE SOLID PARTICLE EROSION OF TUNGSTEN CARBIDE IN SILICON CARBIDE SLURRY

by

Michael John Sandstrom

A thesis submitted to the faculty of
The University of Utah
in partial fulfillment of the requirements for the degree of

Master of Science

Department of Mechanical Engineering

The University of Utah

December 2003

ABSTRACT

The objective of this study was the examination of erosion rates of tungsten carbide using a high velocity slurry flow where the velocity, impingement angle, and number of particles are controlled. The apparatus used for these experiments was an impinging jet of high velocity slurry flow of silicon carbide particles. The fluid velocity in this study was varied from 70 – 200 ft/sec and the impingement angle was varied from 10 – 90 degrees. Five grades of tungsten carbide were examined along with a control batch of 1018 mild steel. The erosion was caused by silicon carbide particles of 280 and 320 mesh densities. The results of the study were plotted using a calculated erosion coefficient that was defined as the ratio of the mass of material removed from the samples divided by the mass of silicon carbide particles. Algebraic equations in terms of velocity and impingement angle were determined that fit the experimental data.

TABLE OF CONTENTS

LIST OF FIGURES

LIST OF TABLES

ACKNOWLEDGEMENTS

I would like express my thanks to the following individuals for their assistance in helping me complete this project.

I would like to thank those individuals at Hughes Christensen, especially Alan Sinor, Roy Ledgerwood, and Tim Marvel, for allowing me to pursue this research and providing the necessary funding for me to be able to complete it. Without their support, this project would not have been possible.

I would like to thank Dr. Charles Thomas for his assistance as the chair of my thesis committee. His encouragement and suggestions were very helpful in contributing to the success of this project.

Special thanks needs to go to Dr. Michael Wells for his in-depth knowledge into this field of research. His direction and suggestions were very valuable in the progression of this work. His patience and encouragement were also appreciated as he helped me to complete this research.

I would like to thank Dr. David Hoeppner for taking the time to be on my thesis committee.

I would also like to thank those at Terra Tek, Inc., who provided the facility in which to conduct the experiments.

Last of all I would like to thank my family for having patience, and allowing me to be gone for so much of the time as I worked to complete this project.

CHAPTER 1

INTRODUCTION

The equipment used to drill oil and gas wells in the petroleum industry is often subjected to severe environments that cause erosion to the down hole equipment. Specific materials are typically selected in the manufacturing of these products to help them resist erosion and prolong their economic life. One of the most common materials used in the manufacture of oil well drilling bits to combat erosion is tungsten carbide. Tungsten carbides are manufactured in a vast array of material compositions that vary carbide size, carbide densities, and the use of different materials such as cobalt and nickel that act as binders to hold the carbide particles together.

Tungsten carbide manufactured with different compositions typically exhibits widely different erosion resistant characteristics. The erosion of tungsten carbide is observed to occur chiefly in the small spaces between the tungsten carbide particles. The binding material between the carbide particles is first eroded, exposing the larger particles of tungsten carbide, which are then dislodged, more or less intact. Thus, the physical size of the tungsten carbide particles making up the matrix material, or more specifically the gap between particles, and the composition of the binding material between the tungsten carbide particles tend to control the rate at which material is removed. This, in conjunction with the size of the impinging solid particulate,

determines the relative erosion rate as a function of velocity, impingement angle and particle diameter.

1.1 Definition of Erosion

The purpose of this study is to evaluate the erosion rate of materials by small solid particles entrained in liquid flows. Erosion is generally defined as the process by which material is gradually worn away when exposed to repeated contact by small particles. The rate at which erosion will occur is generally dependent on: 1) the relative velocity of the particles with respect to the impingement surface, 2) the angle of impact between the two materials, 3) the size and shape of the particles, and the material properties of each of the different materials. Some of the material properties that affect the erosion rate are the hardness, strength, ductility and brittleness of the materials involved.

This study is specifically focused on solid particle slurry erosion, or erosion caused by particles carried in the slurry medium. A slurry, in this case, will be defined as a suspension of solid particles in a liquid, which maintains the consistency of a liquid.

1.2 Experimental Procedure

The slurry erosion experiments were conducted by focusing a small diameter submerged jet at tungsten carbide specimens. The high velocity jet impinged a slurry, made up of water and small silicon carbide particles, at the specimens at various velocities and impingement angles. The rate of specimen erosion was computed using the so called erosion factor that is defined as the weight of material removed divided by the weight of erodent particles impinged on the sample.

1.3 Thesis Statement

The objective of this study is to experimentally determine the relative slurry erosion rates of five different tungsten carbide compositions. The functional relationships among the rate of erosion, the relative solid particle velocity and angle of particle impingement are established. Algebraic equations are provided that define the erosion rate for the five compositions plus mild steel in terms of the velocity and impingement angle of the slurry flow.

CHAPTER 2

GENERAL INTRODUCTION AND LITERATURE REVIEW

This chapter will provide a more detailed introduction into the focus of this thesis and outline some of the existing research that has been written about erosion. The last item in this chapter will be an overview on how this thesis research will be accomplished.

2.1 General Introduction

In the petroleum industry, the equipment used to drill oil and gas wells must be strong enough to withstand the high stresses caused by the drilling operation but must also be able survive the severe environment that is created as a result of the drilling. The drilling equipment is continually exposed to high velocity fluid flow of slurries that contain abrasive rock material generated by the drilling process. These conditions can exist for long periods of time and can cause severe deterioration to the quality of the drilling tools through erosive wear. This equipment is typically made of erosion resistant materials to help preserve the equipment from this environment. The most common material used in the manufacturing of drilling bits is tungsten carbide, which is the material examined in this thesis.

A picture of a typical PDC (Polycrystalline Diamond Cutter) drill bit can be seen in Figure 1. These drill bits can be found in a wide range of sizes, from 3 to 30 inches in

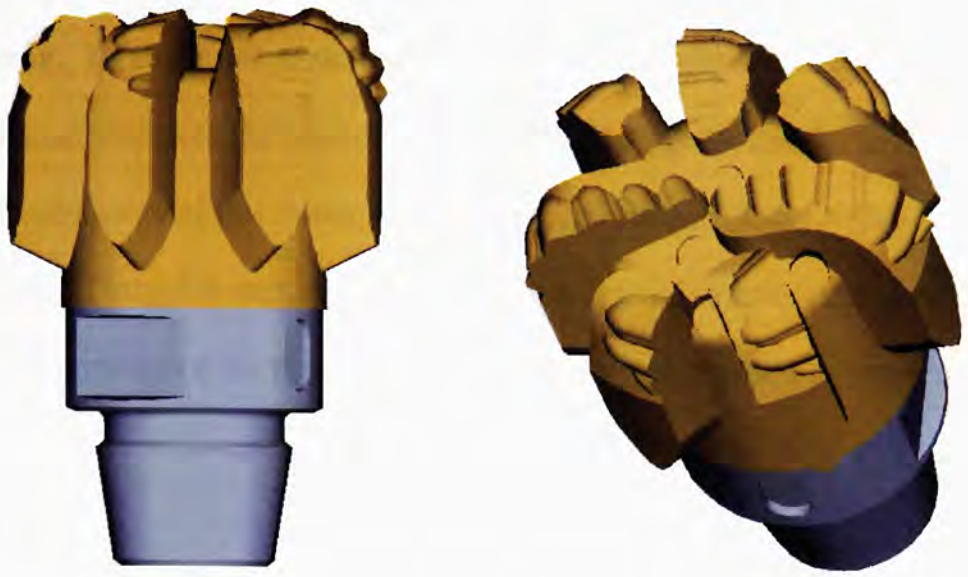

Figure 1. Front and orthogonal view of a typical drill bit.

diameter, and blade configurations. The cutting structure of PDC drill bits consists of diamond faced cutters, mounted on the periphery of the blades. This hard material provides the means for cutting the rock face as the bit rotates and is forced into the rock. All of these bits contain a number of jet nozzles that force high velocity fluid across the face of the bit to clean and cool the cutting structure. Unfortunately, these jets also carry cutting particulates that can erode the bit's surface.

Between the blades on the bit are open areas, junk slots, which allow fluid to circulate through the center and up the sides of the bit. The junk slots generally provide a means for the evacuation of cuttings material away from the cuttings structure. The nozzles are typically located at the beginning of the junk slots, and are arranged to enhance flow directly out of each slot. Since the junk slots house the nozzles, this source of high velocity fluid carrying newly generated cuttings material provides a source for

erosion of the bits face, or bit matrix material. This typically occurs near the jet impingement. To minimize erosion on the bit face, an understanding of the relative erosion characteristics of the materials used in the manufacture of the bit is paramount.

The objective of this thesis is to examine the erosion rates for five different compositions of tungsten carbide that are commonly used to build drill bits. Knowledge of the erosion resistance for these different materials will enable a designer to build bits that will be able to withstand erosive environments.

2.2 Literature Review

The first notable effort to study discrete particle erosion was conducted by Finnie (1). His research was conducted using air to propel small solid particles through a tube at target surfaces and measure the resulting mass loss. Finnie's research was based on the premise that the individual solid particles created a cut in the target material when they came into contact. The resulting cut in the target material was representative of how much of the cross section of each particle penetrated into the target surface.

Finnie established curves to represent the expected erosion rates for both ductile and brittle materials (Figures 2 and 3, respectively). The curves demonstrate the importance of the impingement angle on the resulting erosion rate.

In ductile erosion, the erosion rate reaches a peak at about eighteen degrees and then loses efficiency as the angle becomes steeper. In the brittle erosion curve the erosion rate increases as the impingement angle increases. This would correspond with the increased impact energy caused by the normal impact.

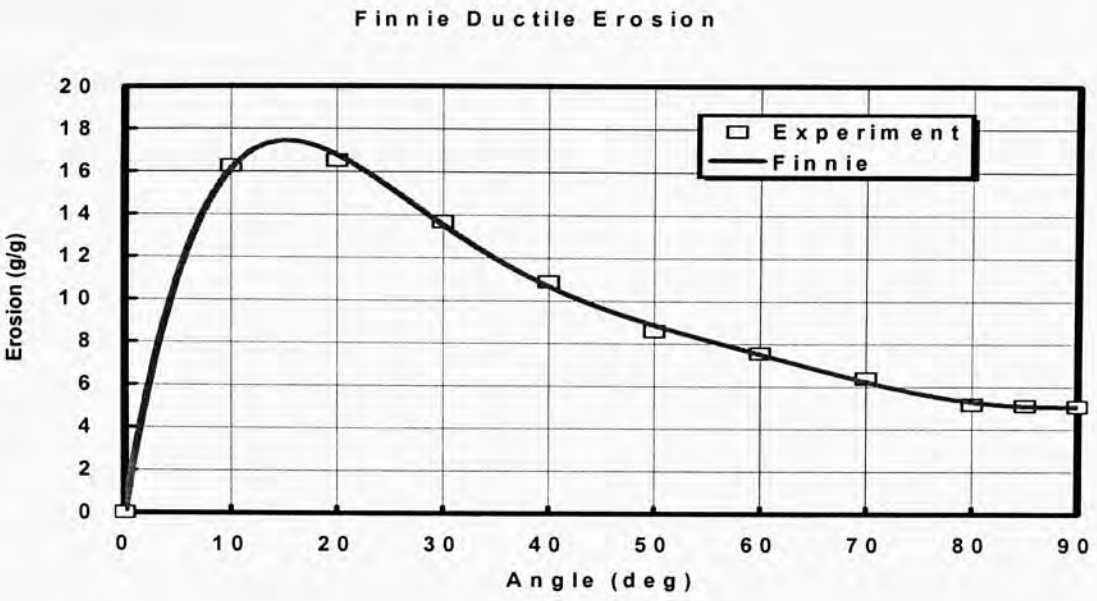

Figure 2. Typical erosion curve for ductile materials developed by Finnie.

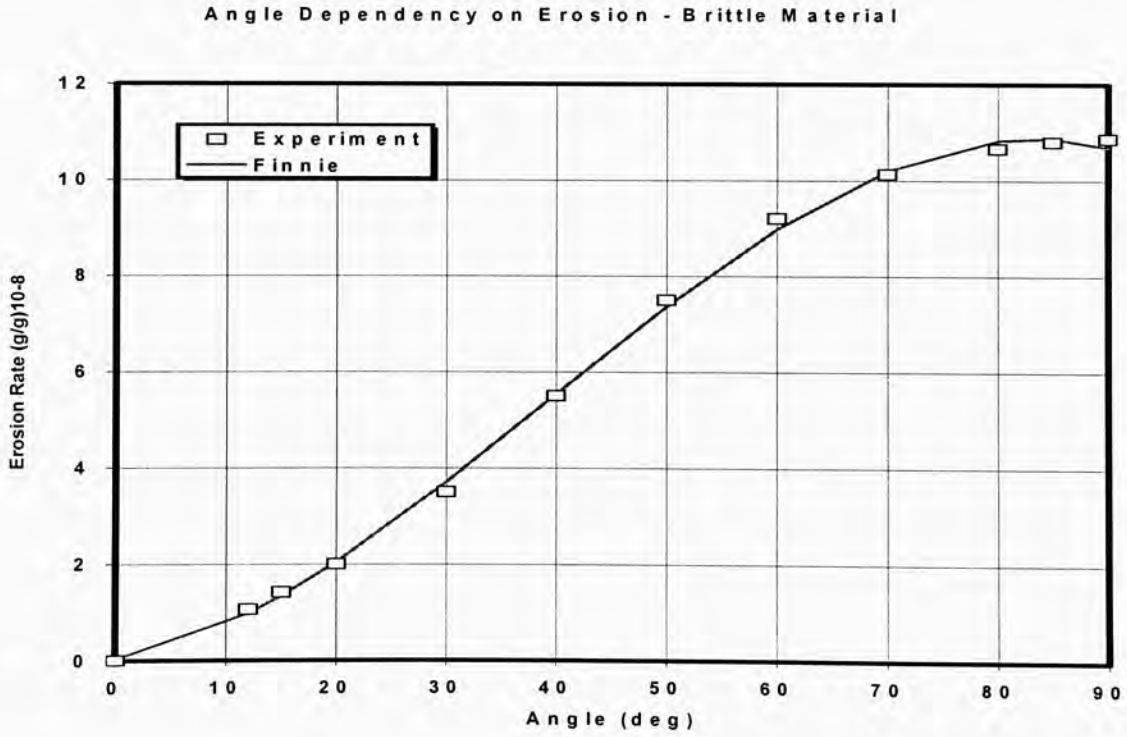

Figure 3. Typical erosion curve for brittle materials developed by Finnie.

2.2.1 Slurry Erosion

Levy (2) extended the classical erosion research by including the study of erosion with the particles dispersed in a slurry. Slurry erosion is erosion that occurs when particles entrained in a fluid cause erosive wear to a base material. Figure 4 is a typical curve that Levy obtained experimentally for a ductile metal that was eroded by slurry. This curve shape is interesting because of the bimodal nature of the curve with a local minimum at around 60° and the local maximum at 42°. In this curve, the erosion rate reaches a maximum at 90° similar to the brittle-erosion curve. The intermediate peak represents the particles ability to penetrate the boundary film that is created by the fluid. Levy observed this intermediate peak in coal/kerosene slurries and water/SiO slurries at low velocity.

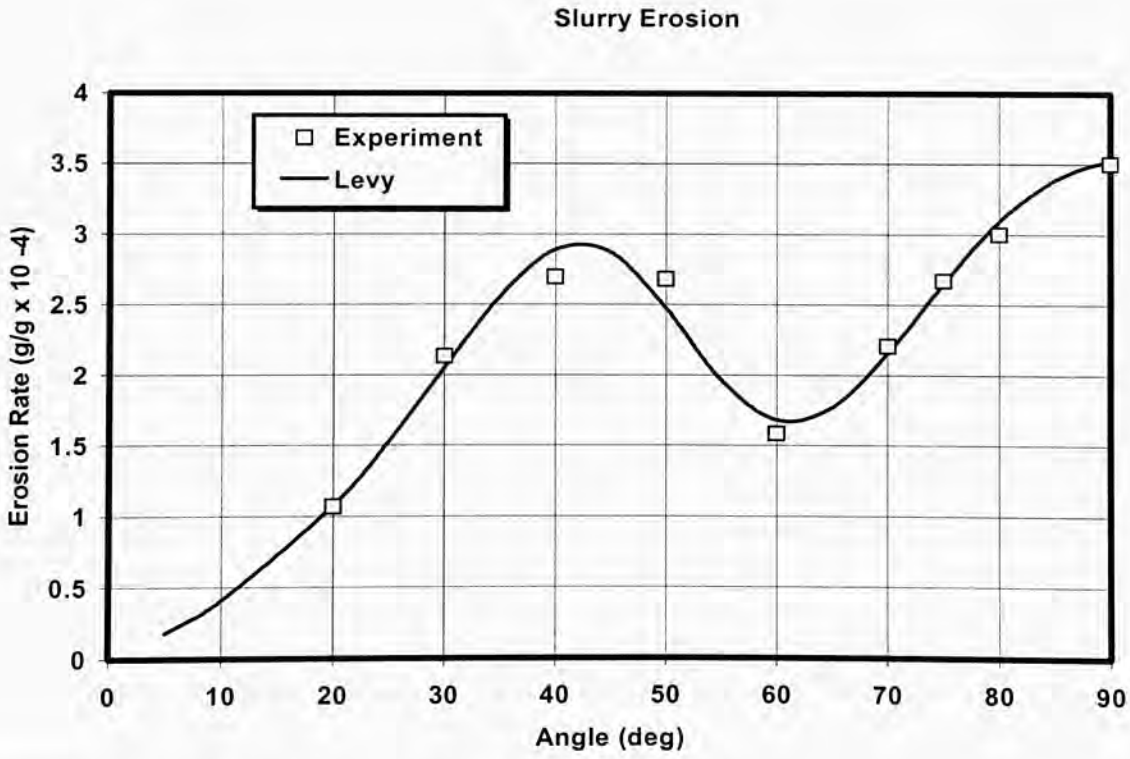

Figure 4. Typical slurry erosion curve developed by Levy.

2.2.1.1 Slurry erosion tester – pot tester. Two different types of experimental testers have been created to analyze slurry erosion. The two types are the pot tester, which will be described in this section, and the jet impact tester, which will be discussed in the next section. The most common is the pot tester. The pot tester consists of a bath of fluid that contains suspended abrasive particles. Measurements are acquired by immersing the erosion sample in the bath of fluid and then spinning the sample in the liquid so that the sample comes in contact with the abrasive particles.

References 3 – 6 contain examples of slurry erosion tests using a pot tester. The information gained from a pot tester is limited due to the constraints of the test. The pot tester is limited in that it is not possible to control the impact angle or the velocity of the individual particles as they contact the target surfaces. It is also difficult to obtain particle impacts if the impact direction does not lie normal to the rotating specimen. If the particles are not in line with the center of the rotating specimen, the particles will often just slide by the surface of the specimen.

2.2.1.2 Slurry jet impingement. The second kind of slurry erosion tester is the jet impact tester. This tester operates by forcing the slurry through a nozzle that accelerates the fluid flow at the target material. The nozzle is used to intensify the energy of the impacting solids. This method more correctly simulates the service application and allows much more accurate control over the particle impact angle and velocity. This is the type of tester that will be used for this research.

Stack and Pungiwat (7) studied the particle size effect for metallics, polymers, and ceramics. The impacting particles that were used for these tests were alumina and silicon carbide, ranging in size from 250 to 1000 μm. The impingement angle was varied from

22.5 to 90°. The testing was done at relatively low velocities of 4, 6, 8, 10, and 11 m/s. Five materials were tested: iron, aluminum, stainless steel, alumina, and Teflon. The interesting result from this research is that the erosion rate peaked at intermediate particle sizes for all the materials except for the ceramic. The particle size where each peak was observed was a function of the different test variables, such as target material, particle properties, and characteristics of the flowing environment.

In Turenne et al. (8), the effect of the sand concentration in the slurry flow was analyzed for its effect on the resulting erosion rate. The velocity was held constant at 17m/s. The sand concentrations that were measured were 1, 5, 10, 15, and 20% wt. The impingement angle was held constant at 90°. The target material was aluminum. The result showed that the erosion rate decreased as the concentration of particles was increased. It was also determined that the rebounding particles were actually interfering with the newly incoming particles. The rebounding particles essentially created a shield that protected the surface from the increased number of particles.

In Wheeler and Wood (9), the solid particle erosion of CVD diamond coatings was measured. CVD is defined as chemical vapor deposition. This is the process of coating a base material with a chemical process. The materials tested included CVD diamond deposited onto tungsten and silicon carbide in thicknesses from 10 – 47μm. The erosion rate was measured using two types of testers that created different ranges of velocities. The first was a water-sand rig that created velocities of 16 and 28 m/s. The second type was an air-sand rig that created velocities of 63, 148, and 268 m/s. The tests were conducted at an impingement angle of 90°. The parts were tested until the CVD coating was penetrated. The result measured in this testing was the time required for the

coating to be penetrated. The eroded surface was also examined by a scanning electron microscope to determine the type and amount of surface degradation due to the erosion.

2.2.2 Erosion of Tungsten Carbides

Very little erosion research has been conducted on tungsten carbide materials. Ninham and Levy (10) investigated the characteristics of erosion with carbides when the carbide density is varied in the matrix. The materials were examined using a gas-blast type instrument. The results showed that the erosion is dependant on the binder material that holds the carbide together. When the impacting particles are able to remove the binder from around the individual carbides, the erosion rates are high. However when the density of carbides is high, the erosion rate is low due to the inability of the impacting particles to remove the binder material.

Ball et al. (11) studied the effect of erosion on hopper valves used in a coal gasification system. Testing was performed using a specially designed rig to simulate temperature, pressure differentials, and valve geometries using a slurry of erosive particles. A number of different materials with varying surface treatments were examined in the study. The result showed that low binder contents and small carbide particles increased the erosion resistance for the valves.

2.2.3 Velocity Exponent

Levy (2) demonstrated the relationship that velocity has on the expected erosion rate in Figure 5. A line has been drawn from erosion rates plotted at different velocities but corresponding impact angles. The slope of the line represents the velocity exponent

associated with the impingement angle for the material. The slope of the line has been shown to vary for different impact angles and different materials.

2.3 Research Overview

In summary, it is evident that the previous studies of solid particle erosion are primarily confined to steel, copper and aluminum alloys. Very little work has been performed using slurries to transport the erodent. Rather, most of the existing erosion data has been obtained from air transported particles. The literature outlines general relationships for the erosion rate of ductile and brittle materials that, for the most part are consistent with all typical alloy metals. In addition, very little work has been done to

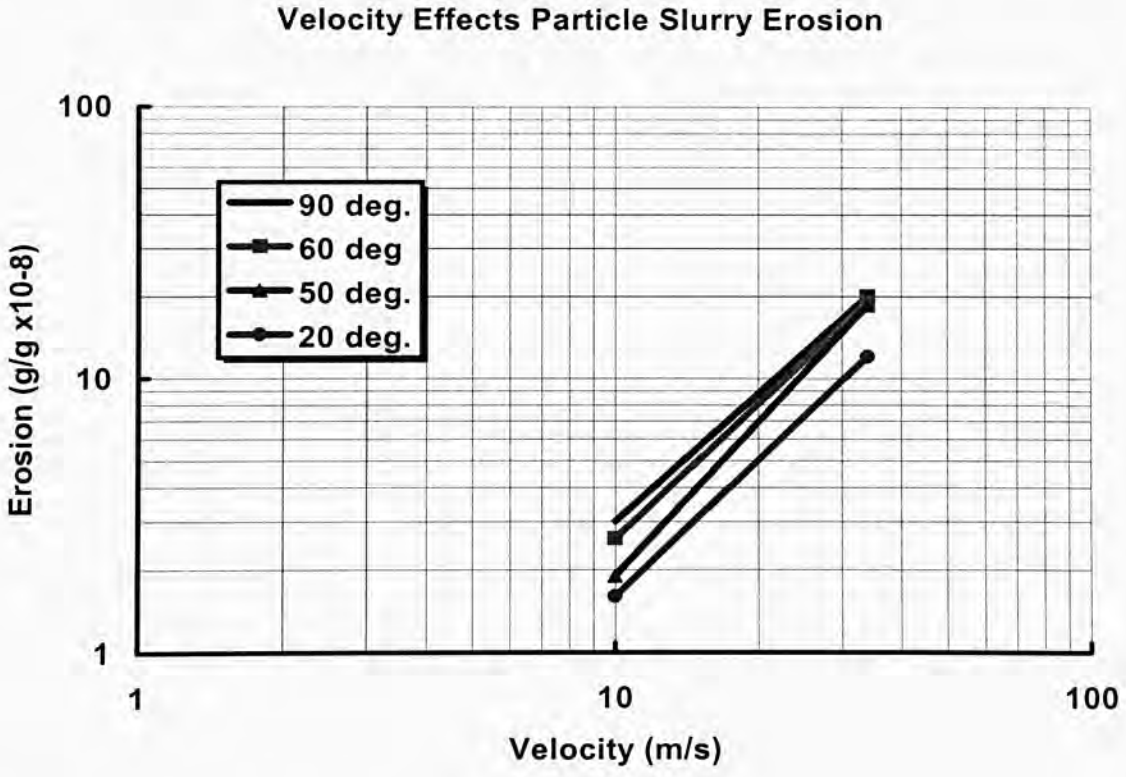

Figure 5. Typical log/log relationship of velocity to erosion results.

examine the results of erosion of tungsten carbides with varying velocities and impact angles.

The focus of this study was to experimentally determine the rates of solid particle erosion of five tungsten carbide materials, and plain carbon steel, when subject to a slurry of silicon carbide particles in water. The high velocity slurry was focused on the test specimen's using a small diameter jet nozzle positioned at roughly 6.8 nozzle diameters from the specimen. The study examined the dependency of the erosion rate on the particle velocity, and impingement angle. Slurry velocities in this study were varied from 70 to 200 ft/sec and the impingement angle varied from 5° to 90° at increments of 5°, 10°, 18°, 45°, 60°, and 90°. The silicon carbide erodent particles were from two different particle size distributions, 280 mesh and 320. These have average particle sizes of 40.72 and 35.35 microns, respectively. Simple algebraic relations are derived describing the rate of erosion for the five tungsten carbide samples and the steel sample.

CHAPTER 3

PROCEDURES, EQUIPMENT, MATERIALS, AND ANALYSIS

Chapter 3 details the methodology used to conduct the erosion rate experiments. The chapter is divided into four sections that describe the Procedure (section 3.1), the Equipment (section 3.2), the Materials (section 3.3), and an Uncertainty Analysis that was performed on the governing equations (section 3.4). Section 3.1 provides an explanation of the procedures used to measure the erosion rates for the six materials evaluated. The tests were performed to obtain data that define erosion rates for each of the material samples.

Sections 3.2 and 3.3 describe the equipment and materials that were used to measure the erosion rate under various conditions of flow rate and particle impingement angle. The equipment section, 3.2, provides a description of the equipment used to conduct these tests. The material section, 3.3, provides information about the different materials used in the tests. The specimens tested include five different grades of tungsten carbide samples, one batch of 1018 steel samples, the silicon carbide particles used to create erosion, and a description of the materials that were used to create the mud slurry.

The mud slurry was used to suspend the silicon carbide in a fluid medium so that it could be pumped through the system.

The last section, 3.4, provides an experimental uncertainty analysis. The experimental uncertainty was computed using standardized ASME methods (12).

3.1 Procedures for Measuring Erosion

The erosion rate measured for the different tungsten carbide materials was obtained at various velocities and impact angles. The erosion rate is typically expressed in terms of an erosion factor or coefficient. This erosion factor is defined as a ratio of the mass of material that is lost from a sample, divided by the mass of material (erodent) that comes in contact with that sample. This relationship is shown in Eq. 1.

$$\varepsilon = \frac{\text{Mass loss from target sample} \quad \text{(grams)}}{\text{Mass of impacting material} \quad \text{(grams)}} \tag{1}$$

Generally, the erosion factor is a function of the physical properties of the specimen, the physical properties of the erodent particles, the size and shape (angularity) of the erodent, the particle impingement angle, the particle impingement velocity and the flow medium used (typically air or water). For the experiments described in this thesis, only the physical properties of the specimens, the particle impingement velocity and the particle impingement angle were varied. Curves were then fit through the acquired erosion data for each specimen, plotting the erosion factor against the impingement angle in one case and the impingement velocity in another. A characteristic shape for these curves was identified and compared to those given in the literature review.

Typically, the determination of the effect of impact angle on the erosion rate is considered one of the most fundamental mechanisms of erosion. In Chapter 2, various general relationships from the literature were shown that illustrate the functional relationship between the erosion factor and the angle of particle impingement. Specifically, the original data by Finnie (1) showed different relationships between the erosion factor and the impingement angle for ductile specimens, Figure 2, and for brittle specimens, Figure 3. It should be noted that these curves were defined from experiments that used erodent particles in an air stream. In addition, some investigators (2) have measured bimodal curves describing the angle dependency on the erosion factor, specifically for slurry erosion, Figure 4. This bimodal relation was measured using steel specimens eroded by relatively soft coal particles at velocities around 30 m/s. Using the harder SiC particles and higher velocities, approximately 60 m/s, no such bimodal distribution was seen in the present experiments. The fundamental goal of this research was to define the characteristic curves describing the angle dependency on erosion for solid particle erosion of slurries at high velocities. As a baseline, erosion curves were first established using ductile, 1018, mild steel to compare this with those found in the literature, in particular with the curve measured by Levy (2) (See Figure 4).

The tests were conducted at a selected range of impact angles to fully define the shape of the erosion rate vs. impingement angle curve. Tests were also conducted at different velocities to: 1) determine if the curve shapes are consistent at all velocities and 2) determine the velocity exponent describing the velocity dependency on the erosion rate. The erosion behavior of the steel was then compared with the batches of tungsten carbide samples.

The impact angles evaluated in these experiments were 5, 10, 18, 45, 60, and 90°. Typical jet spread characteristics rendered the measured erosion rate at 0° of little value, since the normal spread of the jet forced particles to impinge on the specimens at greater than zero angles. The angles were chosen so that the typical Finnie ductile and brittle distributions, as well as the bimodal distribution of Levy, could be identified. For example, the 60° degree test angle was chosen because this is in the proximity of the local minimum value that is found in the bimodal curves published by Levy. Once the angle dependency on the erosion rate was established, offsetting tests were performed at 45 and 90°. The velocity of the majority of the tests was performed at 200 ft/s (60.96 m/s). Additional tests were performed at 100 ft/s (30.48 m/s) to determine the velocity effect on the erosion rate.

3.2 Erosion Test Equipment

This section describes the experimental apparatus used for the tests. Figure 6 is a schematic of the test equipment showing the general flow of particles throughout the system.

Hydraulic power is supplied to the system by a triplex Cat Pump, Model 57. This pump has a fixed displacement of 10 gallons per minute and was used to pump tap water from a large storage tank. Downstream from the triplex pump was a pulsation dampener, used to minimize pressure fluctuations in the pressure line during the tests. The triplex pump was used to provide high fluid pressure to the nozzle. This nozzle was also used to focus the particle stream at the erosion specimens. The flow rate from the triplex pump could be varied by diverting flow from the pump through a control valve.

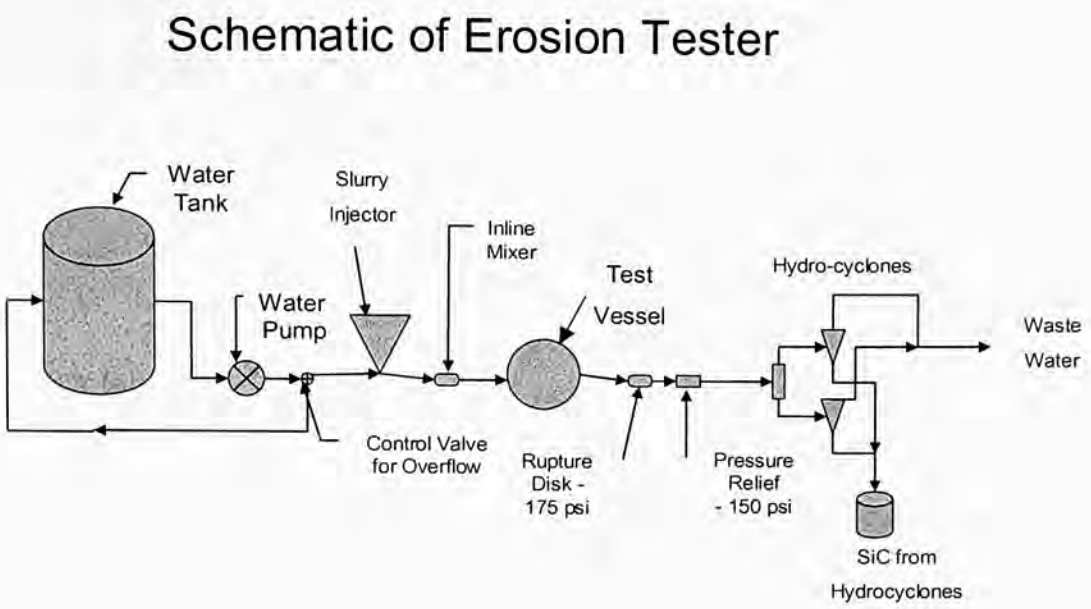

Figure 6. Schematic representation of the test equipment.

Figure 7 is a drawing of the test vessel. The test vessel is designed to hold a test sample at a distance of .850" (21.59mm) horizontally from the nozzle jet. The test samples are circular discs, 1.5" (38.1 mm) diameter and .25" (6.35 mm) thick, cut from single tungsten carbide castings. Typically, erosion rates were such that both sides of a sample could be used for testing. The sample holder is constructed with a circular recess that created a compression fit around the sample. The sample holder is built in the shape of a cylinder so that the sample holder can be rotated to change the impact angle.

The nozzle is made from cubic boron nitride, which is known for its erosion resistance. The nozzle is constructed using a smooth transition to an orifice diameter of .125" (3.175mm) ID. The nozzle orifice was checked regularly to assure that the nozzle opening was not enlarged due to erosion from the fluid flow during the testing.

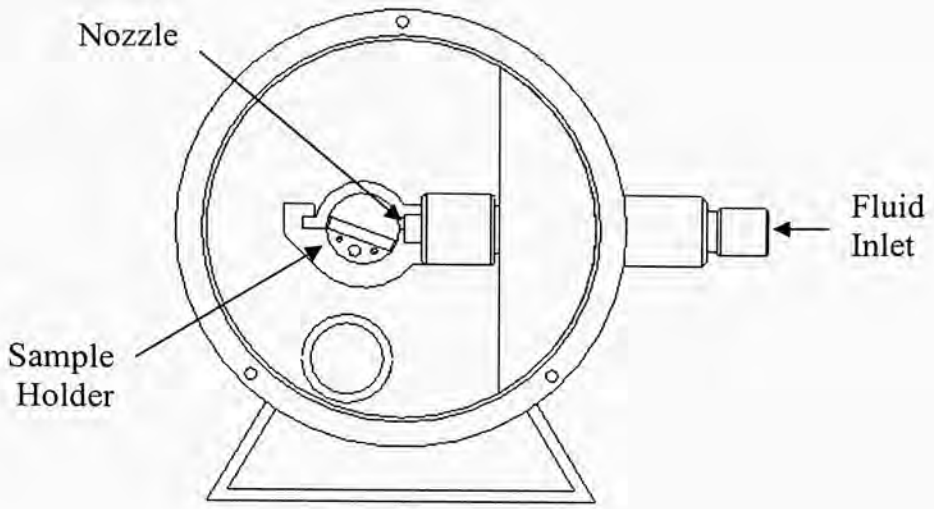

Figure 7. The erosion test vessel.

The test vessel was also designed to hold thin strips of aluminum against the inside wall. These aluminum strips were used to measure the angle at which the particles reflected off of the sample after impact. The rebounding particles etched a mark in the soft aluminum after repeated impact during a test. The etched line was used to calculate the reflection angle of the particles leaving the test sample.

3.2.1 The Particle Injection Pump (PIP)

A specially designed Particle Injection Pump (PIP) was used to force particles into the high pressure fluid flow just upstream of the nozzle, Figure 8. The PIP pumps a slurry of abrasive particles under high pressure into the main nozzle stream using a system of hydraulic cylinders. The PIP is composed of basically two different subsystems. The first subsystem provides power or driving force to the PIP. The power side of the PIP consists of a hydraulic cylinder driven by a separate hydraulic power unit

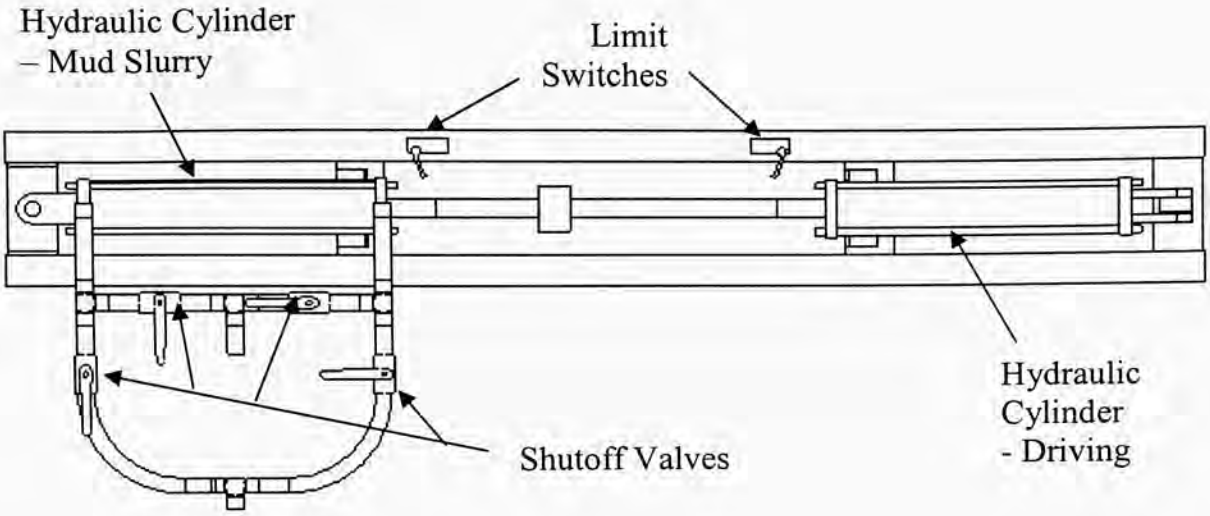

Figure 8. The particle injection pump (PIP).

that forces the cylinder to oscillate back and forth by way of a control valve and directional switches. The driving hydraulic cylinder is then connected to a second hydraulic cylinder by a solid rod, used to pump the abrasive slurry into the fluid system.

The travel of the driving hydraulic cylinder is controlled by limit switches that are mounted in proximity to the connecting rod between the cylinders. The limit switches are placed so that the pump will move the hydraulic cylinder in one direction until the coupler on the connecting rod makes contact with one of the switches. The switch then prompts the control valves to toggle its direction to direct flow through the opposite end of the driving cylinder, causing motion in the opposite direction.

Pumping action of the mud slurry hydraulic cylinder is accomplished by using a series of shutoff valves that control the direction of the slurry flow through the hydraulic lines. Figure 9 is a schematic of the required shut off valve positions allowing fluid to be

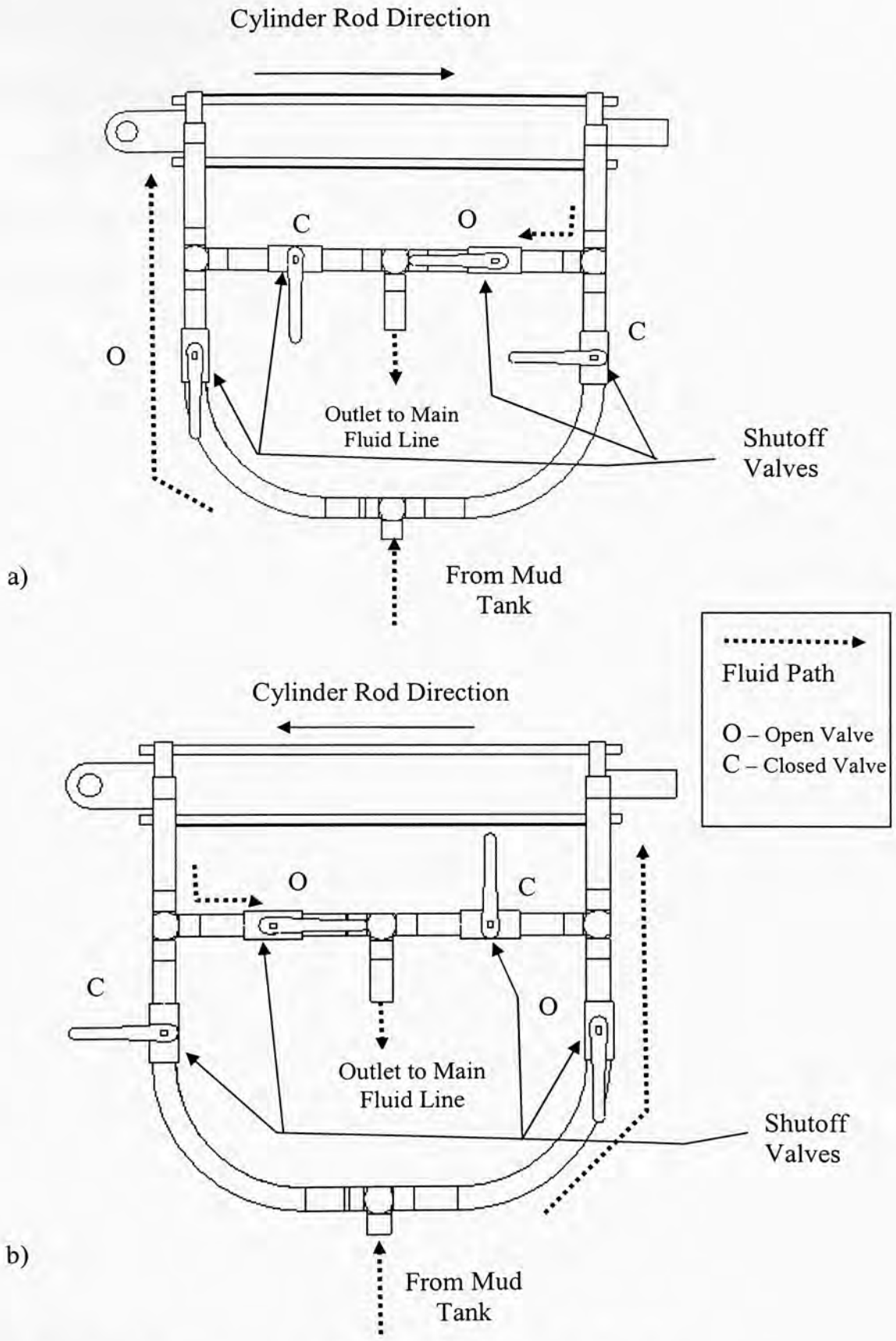

Figure 9. Shutoff valve position for fluid flow in the shown directions.

changed to the opposite position for flow in the new direction. Thus, as the cylinder oscillates the mud slurry is forced into the main fluid line.

In Figure 9, the two pictures, Figures 9a and 9b, represents the shutoff valve positions for flow when the cylinder is moving in opposite directions. The dashed line represents direction of fluid flow in the hoses with the shut off valves in these positions.

Once the slurry has been forced into the main fluid line, it is mixed with the flow from the triplex pump by the use of an inline mixer. The inline mixer consists of a series of vanes that folds the fluid over on itself repeatedly dispersing the abrasive particles into the main fluid flow of the system. It was desired to keep the concentration of erodent particles in the slurry below 2% to reduce the particle-to-particle interaction which could decrease the efficiency of the particle impact on the target samples. This effect was identified by Turenne et al. (8). In their research they recognized that when the concentrations of erodent particles are high they tend to act as a shield and protect the surface from erosion. It is important to note that the measurements of interest were the mass of material removed from the test specimens under specified conditions, and the mass of particles impinged on their surfaces. It is not necessary that the flow of particles through the jet be continuous or uniform. It is only desired that the erodent particle concentration be maintained low enough to minimize particle to particle interaction. This is achieved at or below the 2% slurry concentration.

3.2.2 System Control

Pressure gages on either side of the nozzle are used to monitor the pressure in the fluid lines. The required erodent particle velocity can be determined from the maintained pressure drop across the nozzle.

Flow through the nozzle is obtained using the well-established nozzle equation Eq. (2). The required pressure drop across the nozzle, at a given flow velocity, is obtained by rearranging the terms in Eq. (2) and shown in Eq. (3), The flow coefficient given in the equations was experimentally determined to be 0.97 by making careful flow measurements at a constant rate of flow while monitoring the pressure drop across the nozzle. Particle density was kept below about 2% by weight, thereby minimizing the density effect on the velocity determination.

$$V = K\sqrt{\frac{2\Delta p}{\rho}} \tag{2}$$

$$\Delta p = \frac{V^2 \rho}{2K^2} \tag{3}$$

V = Velocity - m/s (ft/s)
K = Flow Coefficient
Δp = pressure drop (psi)
ρ = slurry density (mass/vol)

3.2.3 System Safety

Rupture disks are used in the fluid lines as a safety precaution against the occurrence of dangerously high pressure levels. The rupture disks are placed in three locations in the system each having a different pressure limit. These locations are: 1) the inlet/outlet side of each of the ports on the slurry cylinders (set to rupture at 575 psi), 2)

in the main fluid line upstream of the test vessel (set to rupture at 700 psi), and 3) downstream of the test vessel (set to rupture at 250 psi). Each of these pressure settings was selected to maintain the pressures inside the various pieces of experimental apparatus and keep them within safe operating levels.

3.3 Materials Used to Create Erosion

There are two categories of materials used in the experiments. The first category includes the materials being eroded. This category includes the five tungsten carbide material samples that are being studied in this research and samples of 1018 steel. The second category is the particles that were used to create the erosion.

3.3.1 Tungsten Carbide Samples

Five different types of tungsten carbide were studied in this research. Pictures of the individual samples showing grain size and density are shown in Figure 10. These materials will be referred to as Types A through E for this research. A brief description of each material as well as the measured density for each material is found in Table 1. All five material samples used an identical nickel manganese bronze alloy for the binder.

The density of each of the tungsten carbide materials was experimentally determined by measuring the volume of displaced ionized water for each sample. The displaced volume in conjunction with the measured weight of each sample was then used to calculate the density.

All of the specimen samples were sized to fit into the experimental testing fixture, 1.5" (38.1 mm) diameter and .25" (6.35 mm) thick. An additional group of samples of

Table 1. Material properties for tungsten carbide samples.

Types	Descriptions	Density (g/cm^3)
A	Fine Grained Cast Tungsten Carbide	13.0580
B	Fine Grained Macrocrystalline Carbide	12.6255
C	Coarse grained Cast Tungsten Carbide	12.3470
D	Medium/Coarse Grained Cast Tungsten Carbide with Iron Powder	10.188
E	Fine Grained Macrocrystalline Carbide	12.4895

1018 steel, having the same size, was used during initial setup and as baseline data for the erosion study.

3.3.2 Silicon Carbide Particles

Two different sizes of silicon carbide particles were used in this research. The size distributions correspond to standard mesh sizes of 280 and 320. The particles size distributions for these mesh sizes are summarized in Table 2. The density of the SiC is 3.2 g/cm^3 and the diameter is nearly spherical.

The difference between the two particle size distributions amounted to a 5.37 μm difference in the average particle diameters in each distribution. The erosion rate with the different particles size distributions were compared to see if there was appreciable difference in the erosion rates. Due to the small variance in the size of the particle diameters, the differences in the resulting erosion rates were negligible.

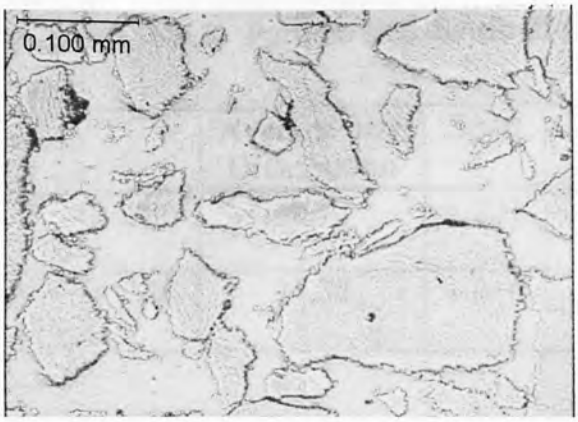

Sample A.

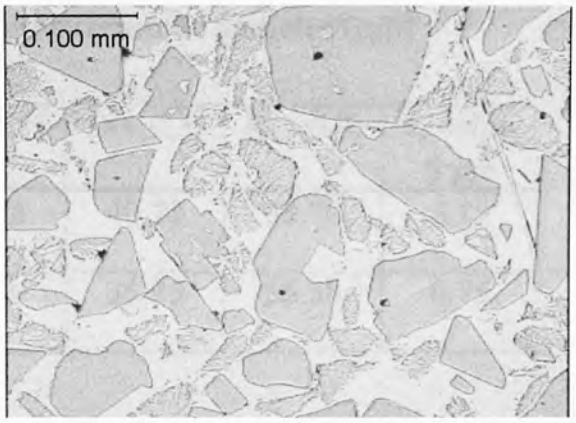

Sample B.

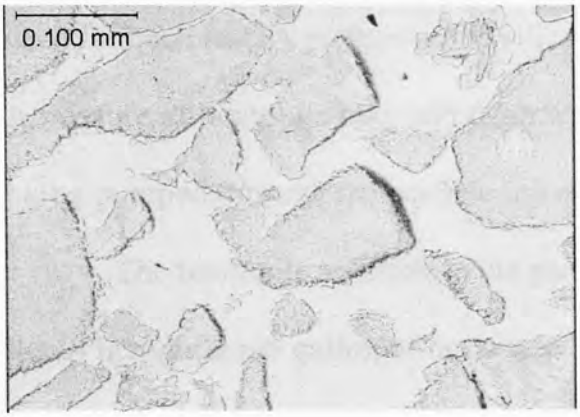

Sample C.

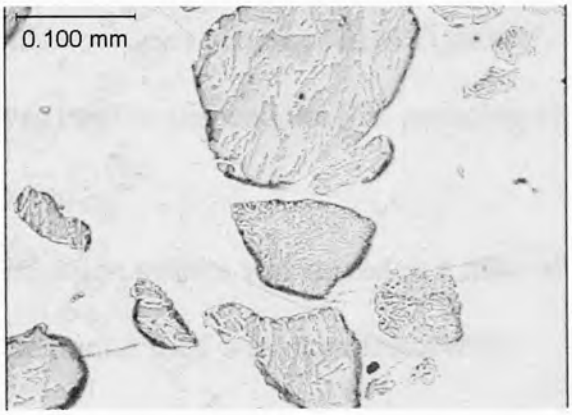

Sample D.

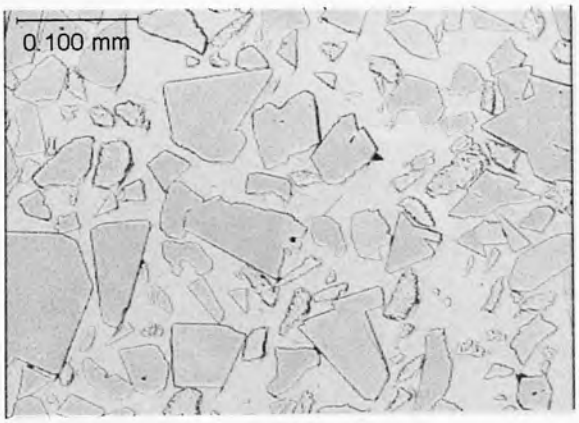

Sample E.

Figure 10. Tungsten carbide samples for study.(All images were photographed at 100X magnification.)

Table 2. Particle size distribution of silicon carbide particles (μm)

	Average Size Distribution	Span	D(v,0.1)	D(v,0.5)	D(v,0.9)	% below 6 μm
280	40.72	1.227	19.72	40.72	69.70	2.19
320	35.35	1.016	20.69	35.35	56.58	0.75

Therefore there will not be a distinction drawn between which mesh distribution was used for each test. A picture of the silicon carbide particles can be seen in Figure 11. A mixture of bentonite clay and fresh water was used to suspend the SiC particles while being pumped through the particle injection pump.

The bentonite solution in the particle injection system was mixed in a ratio of .36 lbs of bentonite per gallon of tap water. The bentonite used was manufactured by

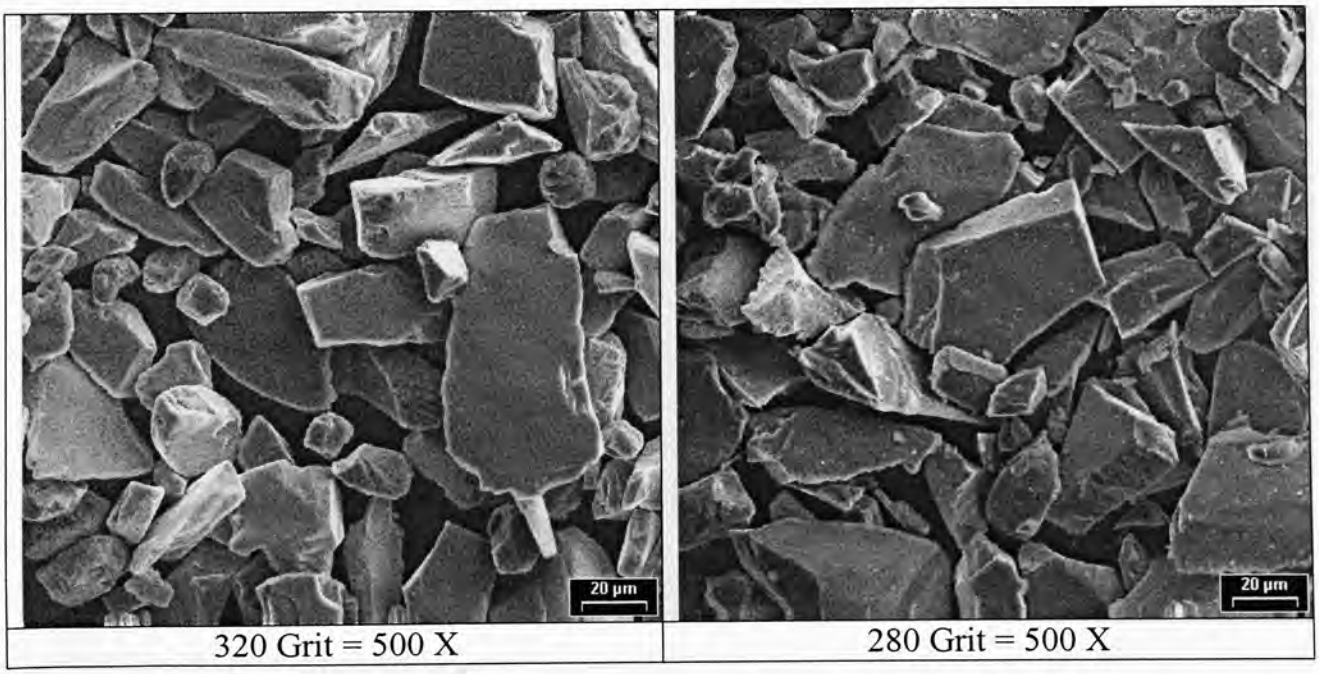

320 Grit = 500 X | 280 Grit = 500 X

Figure 11. Microscopic view of silicon carbide particles from 320 and 280 grit mesh distributions.

CETCO and was labeled Super Gel X. Settling tests were conducted to determine the minimum bentonite concentration that would support the silicon carbide particles. To build sufficient viscosity to suspend the silicon carbide particles, it was necessary to hydrate the bentonite before use. Due to the time required for the mud to hydrate, the bentonite particle slurry was generally mixed in large enough quantities to provide slurry for multiple tests.

The rheology of the bentonite solution was measured prior to use. The solution density in the primary jet stream just upstream of the particle injection was used in the calculation to determine the pressure drop for each velocity requirement. The average density for each batch was found to be approximately 64.0 lbs./gal. The quantity of bentonite added to the main flow system was insignificant.

3.4 Uncertainty Analysis

An uncertainty analysis is a systematic procedure that provides a predictable estimate of the variance in the experimental measurement. The general form of the equation used to compute experimental uncertainty is given in Eq. 4. The uncertainty is determined by taking the partial derivates of the governing equation with respect to the individual variables then multiplying that by an expected variance in that variable. Finally the square root of the sum of squares of the individual uncertainty values provides an estimated variance for the calculated parameter in the equation. The method provides a ready technique to determine which of the variables is responsible for the highest variability in the governing equation.

$$\omega_x = \left[\left(\frac{\partial x}{\partial a} \omega_a \right)^2 + \left(\frac{\partial x}{\partial b} \omega_b \right)^2 + \left(\frac{\partial x}{\partial c} \omega_c \right)^2 + \ldots \right]^{1/2} \quad (4)$$

In section 3.4.1, a description is provided of the procedure used to measure the nozzle flow coefficient and compute the uncertainty of the nozzle flow coefficient. In section 3.4.2 the uncertainty is calculated for the velocity through the nozzle.

3.4.1 Uncertainty Analysis of the Nozzle Flow Coefficient

The flow coefficient for the nozzle was measured experimentally by pumping tap water through the nozzle at a predetermined pressure drop and measuring the time required to fill a measured volume of water. With the results, it was possible to back calculate the value for nozzle flow coefficient (K) using the nozzle equation Eq. 2. The measured data and calculations are shown in the Appendix.

$$K = \frac{V_o}{\sqrt{\frac{2\Delta p}{\rho}}} \quad (5)$$

Substituting in an equivalent form of the velocity equation (Eq. 6), yields Eq. 7, which is the nozzle equation solved for the nozzle coefficient using values obtained through the experimental procedure.

$$V_o = \frac{\forall}{tA_o} \quad (6)$$

$\forall$ = Volume (ft^3)
t = time (seconds)

A_o = nozzle cross sectional area (ft^2)

$$K = \frac{\frac{(\forall)}{tA_o}}{\sqrt{2\frac{\Delta p}{\rho}}} = \frac{\forall}{tA_o\sqrt{\frac{2\Delta p}{\rho}}} \quad (7)$$

V_o = Velocity - m/s (ft/s)
K = Flow Coefficient
Δp = pressure drop (psi)
ρ = slurry density ($slug/ft^3$).

The uncertainty equation for nozzle flow coefficient is given in Eq. (8). Taking the partial derivative of Eq. (7) with respect to the individual variables in the equation yields Eq. 8a – 8e. To evaluate the Eq. 8a – 8e, the following, typical, values are used for the variables in the equations: t=.40 seconds, $\forall$ = .668 ft^3 (= 5 gal), Δp = 40,320 psf (280 psi), ρ=1.94 $slugs/ft^3$, A_o = 8.522E-05 ft^2.

$$\omega_K = \left[\left(\frac{\partial K}{\partial \forall}\omega_{\forall}\right)^2 + \left(\frac{\partial K}{\partial t}\omega_t\right)^2 + \left(\frac{\partial K}{\partial A_o}\omega_{A_o}\right)^2 + \left(\frac{\partial K}{\partial \Delta p}\omega_{\Delta p}\right)^2 + \left(\frac{\partial K}{\partial \rho}\omega_{\rho}\right)^2\right]^{1/2} \quad (8)$$

$$\frac{\partial K}{\partial \forall} = \frac{1}{tA_o\sqrt{\frac{2\Delta p}{\rho}}} = \frac{1}{40(8.522E-05)\sqrt{\frac{2(40320)}{1.94}}} = 1.439 \quad (8a)$$

$$\frac{\partial K}{\partial t} = \frac{-\forall}{t^2 A_o\sqrt{\frac{2\Delta p}{\rho}}} = \frac{-.668}{40^2(8.522E-05)\sqrt{\frac{2(40320)}{1.94}}} = -.024 \quad (8b)$$

$$\frac{\partial K}{\partial A_o} = \frac{-\forall}{tA_o^2\sqrt{\frac{2\Delta p}{\rho}}} = \frac{-.668}{40(8.522E-05)^2\sqrt{\frac{2(40320)}{1.94}}} = -112788.70 \qquad (8c)$$

$$\frac{\partial K}{\partial \Delta p} = \frac{-\forall}{2tA_o\Delta p\sqrt{\frac{2\Delta p}{\rho}}} = \frac{-(.668)}{2(40)(8.522E-5)(40320)\sqrt{\frac{2(40320)}{1.94}}} = -1.19e\text{-}05 \qquad (8d)$$

$$\frac{\partial K}{\partial \rho} = \frac{\forall}{2tA_o\rho\sqrt{\frac{2\Delta p}{\rho}}} = \frac{(.668)}{2(40)(8.522E-5)(1.94)\sqrt{\frac{2(40320)}{1.94}}} = .248 \qquad (8e)$$

Using the calculated values for the partial derivatives and multiplying that by an expected variance in the variable yields the components for the uncertainty equation. This version of the uncertainty equation is found in equation (9). The expected variance of each variable was determined by making estimates and observations into how much each variable could vary. The following terms were used for this variance: $\omega_{\forall} = .01$, $\omega_t = 1$, $\omega_{Ao} = .000001$, $\omega_{\Delta p} = 1440$, $\omega_\rho = .05$.

$$\omega_K = \left[(1.44(.01))^2 + (-.024(1))^2 + (-11278.7(.000001))^2 + (-1.19e-05(1440))^2 + (.248(.05))^2\right]^{1/2} \qquad (9)$$

$$\omega_K = .0369 \qquad (9a)$$

Therefore, the uncertainty in the measured flow coefficient is roughly 3.8% of the computed value of 0.96. Analyzing Eq. 9, all of the variables except the volume contribute relatively equally to the uncertainty of the flow coefficient.

3.4.2 Uncertainty Analysis of the Nozzle Equation

An uncertainty analysis was performed on the nozzle equation (Eq. 2) which is rewritten below for convenience. Taking the partial derivative of the nozzle equation with respect to each variable, and then evaluating gives Eq. 10. To evaluate Eq. 10, the following typical values are used for the variables: K = .96, Δp = 40,320 psf (280 psi), ρ= 1.94 slugs/ft^3. The evaluations of the partial derivatives for the variables in Eq. 10 are given in Eq. 10a – 10c.

$$V_o = \mathrm{K}\sqrt{\frac{2\Delta p}{\rho}} \qquad \text{(Nozzle Equation)} \qquad (2)$$

$$\omega_{Vo} = \left[\left(\frac{\partial V_o}{\partial K}\omega_K\right)^2 + \left(\frac{\partial V_o}{\partial \Delta p}\omega_{\Delta p}\right)^2 + \left(\frac{\partial V_o}{\partial \rho}\omega_\rho\right)^2\right]^{1/2} \qquad (10)$$

$$\frac{\partial V_o}{\partial \mathrm{K}} = \sqrt{\frac{2\Delta p}{\rho}} = \sqrt{\frac{2(40320)}{1.94}} = 203.88 \qquad (10a)$$

$$\frac{\partial V_o}{\partial \Delta p} = \frac{\mathrm{K}}{\sqrt{2\Delta p\rho}} = \frac{.96}{\sqrt{2(40320)1.94}} = .0024 \qquad (10b)$$

$$\frac{\partial V_o}{\partial \rho} = \frac{-K}{2\rho}\sqrt{\frac{2\Delta p}{\rho}} = \frac{-.96}{2(1.94)}\sqrt{\frac{2(40320)}{1.94}} = \quad -50.44 \qquad (10c)$$

V_o = Velocity - m/s (ft/s)
K = Flow Coefficient
Δp = pressure drop (psi)
ρ = slurry density (mass/vol).

Estimates of the experimental uncertainties associated with each variable are: $\omega_K = 0.0369$, $\omega_{\Delta p} = 2880$, $\omega_\rho = .05$. Then substituting Eq. 10a-10c into the general form of the uncertainty equation, Equation 10, with the above estimated experimental uncertainties for each parameter gives:

$$\left(\frac{\partial V_o}{\partial K}\omega_K\right)^2 = (203.88 * .0369)^2 = 56.60 \qquad (11a)$$

$$\left(\frac{\partial V_o}{\partial \Delta p}\omega_{\Delta p}\right)^2 = (.0024 * 2880)^2 = 47.78 \qquad (11b)$$

$$\left(\frac{\partial V_o}{\partial \rho}\omega_\rho\right)^2 = (-50.44 * .05)^2 = 6.36 \qquad (11c)$$

$$\omega_{Vo} = \left[56.60 + 47.78 + 6.36\right]^{1/2} \qquad (12)$$

$$\omega_{Vo} = 10.52 \text{ ft/sec} \qquad (12a)$$

From Eq. 11a – 11c, it is clear that all of the variables have relatively the same magnitude of impact on the uncertainty in the velocity through the nozzle. The uncertainty in the nozzle velocity computed directly from the measured data is 5.26%.

CHAPTER 4

EXPERIMENTAL RESULTS

Chapter 4 presents the experimental results from the erosion tests performed during this research. The experimental results are presented in three sections. The first section, 4.1, presents both a table and the corresponding graph of the measured erosion coefficients for the individual tests for each of the erosion samples. The chart plots the erosion coefficient vs. the corresponding impact angle used for each test.

Section 4.2 presents data used to determine the functional dependency of particle impingement velocity on the erosion rate. These data consist of values of the erosion coefficients at a particular impact angle plotted for different velocities in log/log coordinates. The slope of the line is then used to determine the characteristic power law exponent relating impact velocity to erosion rate. The last section, 4.3, of this chapter shows photographs of the characteristic erosion patterns generated on the individual test samples used in the experiments. These samples are grouped by impact angle. The pictures show the shape and size of the resulting cavity that is created by the impacting silicon carbide particles.

4.1 Erosion Test Results

This section contains the measured erosion coefficients from the individual erosion tests. The erosion coefficient is calculated by dividing the mass loss from the test samples by the total mass of the impacting silicon carbide particles (Chapter 3).
The tables of the measured data show the mass loss of the specimen versus the mass of impinging SiC particles for different impingement angles. To the right of the mass loss results are calculated erosion coefficients represented by the symbol ε_1, ε_2 and ε_3 where the subscripts (1, 2, and 3) correspond to the first, second and third consecutive tests performed on the same sample. The data are also segregated with respect to impingement velocity. Most of the tests were performed using impingement velocities of 200 ft/sec and 100 ft/sec, and some data is included using 70 ft/sec. The results are then plotted in charts showing the effect of impact angle on erosion rate under each of the conditions. The following tables and figures show the results for the erosion tests on the steel and tungsten carbide material samples, types A - E respectively. (See Table 3, Figure 12, Table 4, Figure 13, Table 5, Figure 14, Table 6, Figure 15, Table 7, Figure 16, Table 8, Figure 17.)

4.2 Velocity Exponent Data

The data plotted in the Figures 18 – 22 show selected results from the erosion test experiments used to evaluate the dependency of particle impingement velocity on the rate of erosion. The results shown are erosion rates measured at different particle impact velocities that correspond to two impact angles, 45° and 90°. A linear log/log relationship is assumed based on prior data found in the literature and the results of these

Table 3. Test results for the 1018 mild steel erosion tests.

200 (ft/sec)			1st Test			2nd Test
Impact Angle	Sample Mass Loss (g)	SiC Mass (g)	ε_1	Sample Mass Loss (g)	SiC Mass (g)	ε_2
5	0.1505	3171.3	4.7457E-05	0.1688	3171.3	5.3227E-05
10	0.1779	3171.3	5.6097E-05	0.1646	3171.3	5.1903E-05
18	0.1932	3171.3	6.0921E-05	0.1905	3171.3	6.0070E-05
45	0.2773	3171.3	8.7440E-05	0.2771	3171.3	8.7377E-05
60	0.3167	3171.3	9.9864E-05	0.3160	3171.3	9.9644E-05
90	0.3254	3171.3	1.0261E-04	0.3374	3171.3	1.0639E-04
100 (ft/sec)						
Impact Angle	Sample Mass Loss (g)	SiC Mass (g)	ε_1	Sample Mass Loss (g)	SiC Mass (g)	ε_2
18	0.0474	3171.3	1.4947E-05	0.0504	3171.3	1.5893E-05
45	0.0661	3171.3	8.8186E-06	0.0689	3171.3	2.1726E-05
90	0.0846	3171.3	2.6677E-05	0.0819	3171.3	2.5825E-05
70 (ft/sec)						
Impact Angle	Sample Mass Loss (g)	SiC Mass (g)	ε_1			
45	0.0393	3171.3	1.2392E-05			

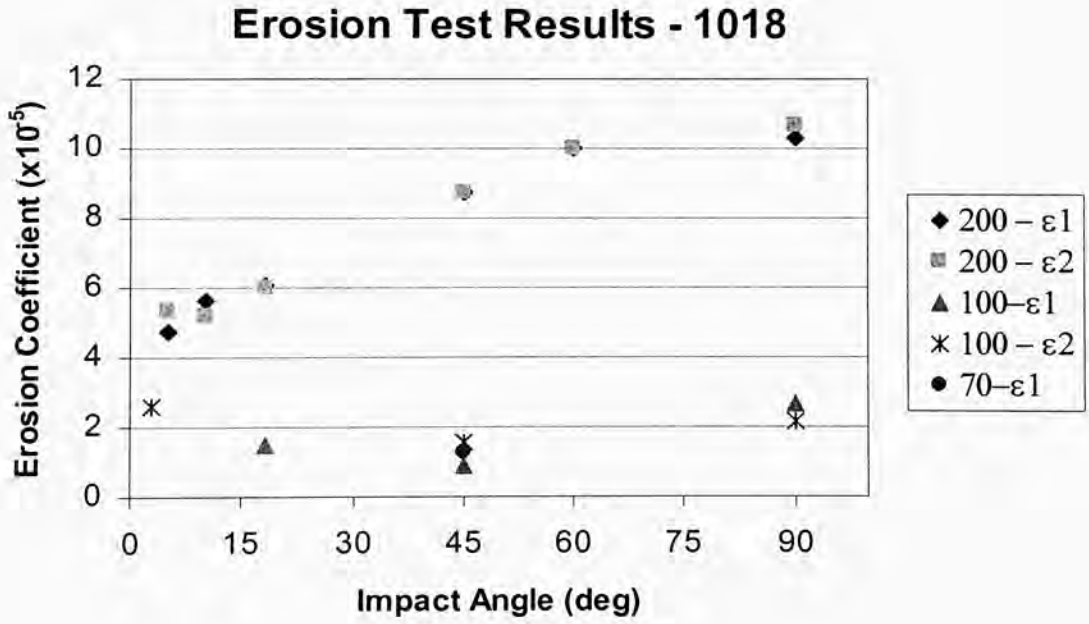

Figure 12. 1018 steel material erosion results plotted vs. the impact angle.

Table 4. Test results for the Type A material erosion tests.

200 (ft/sec)			1st Test			2nd Test
Impact Angle	Sample Mass Loss (g)	SiC Mass (g)	ε_1	Sample Mass Loss (g)	SiC Mass (g)	ε_2
10	0.0577	2268.0	2.5441E-05	0.0483	2268.0	2.1296E-05
18	0.0686	2268.0	3.0247E-05	0.0628	2268.0	2.7690E-05
45	0.0995	2268.0	4.3871E-05	0.0875	2268.0	3.8580E-05
45	0.0945	2268.0	4.1667E-05	0.0826	2268.0	3.6420E-05
60	0.1067	2268.0	4.7046E-05	0.0942	2268.0	4.1534E-05
90	0.1210	2268.0	5.3351E-05	0.1097	2268.0	4.8369E-05

100 (ft/sec)			
Impact Angle	Sample Mass Loss (g)	SiC Mass (g)	ε_1
45	0.0320	3628.7	8.8186E-06
90	0.0374	3628.7	1.0307E-05

70 (ft/sec)			
Impact Angle	Sample Mass Loss (g)	SiC Mass (g)	ε_1
45	0.0223	3628.7	6.1455E-06

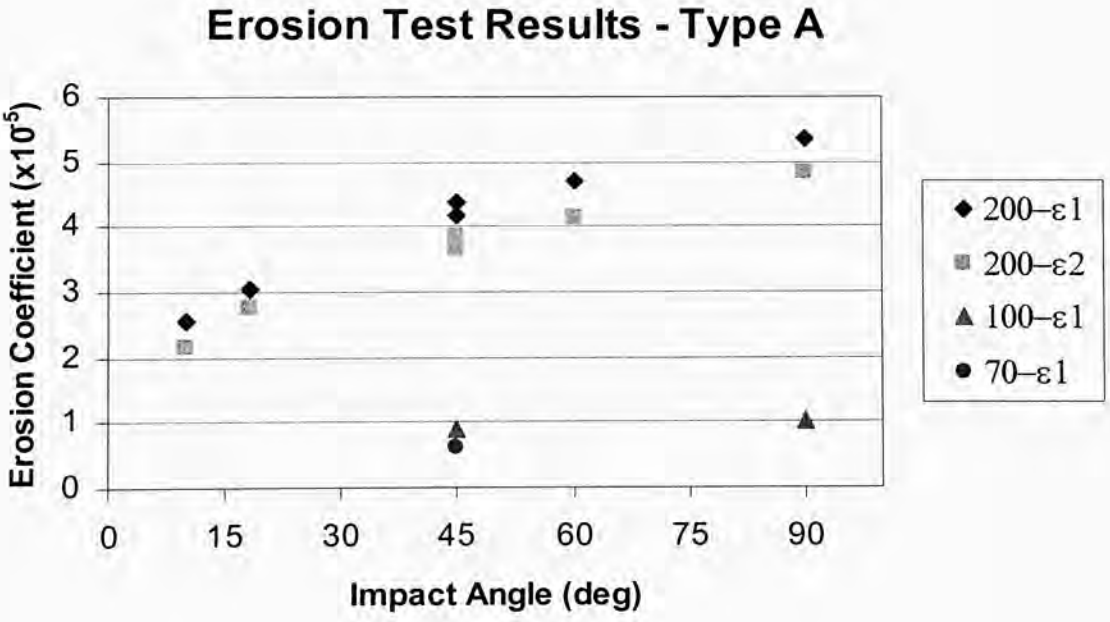

Figure 13. Type A material erosion results plotted vs. the impact angle.

Table 5. Test results for the Type B material erosion tests.

200 (ft/sec)			1st Test			2nd Test
Impact Angle	Sample Mass Loss (g)	SiC Mass (g)	ε_1	Sample Mass Loss (g)	SiC Mass (g)	ε_2
10	0.0360	2268.0	1.5873E-05	0.0183	2268.0	8.0688E-06
18	0.0447	2268.0	1.9709E-05	0.0236	2268.0	1.0406E-05
45	0.0641	2268.0	2.8263E-05	0.0426	2268.0	1.8783E-05
60	0.0739	2268.0	3.2584E-05	0.0486	2268.0	2.1429E-05
90	0.0762	2268.0	3.3598E-05	0.0492	2268.0	2.1693E-05

100 (ft/sec)			
Impact Angle	Sample Mass Loss (g)	SiC Mass (g)	ε_1
45	0.0256	3628.7	7.0549E-06
90	0.0266	3628.7	7.3304E-06

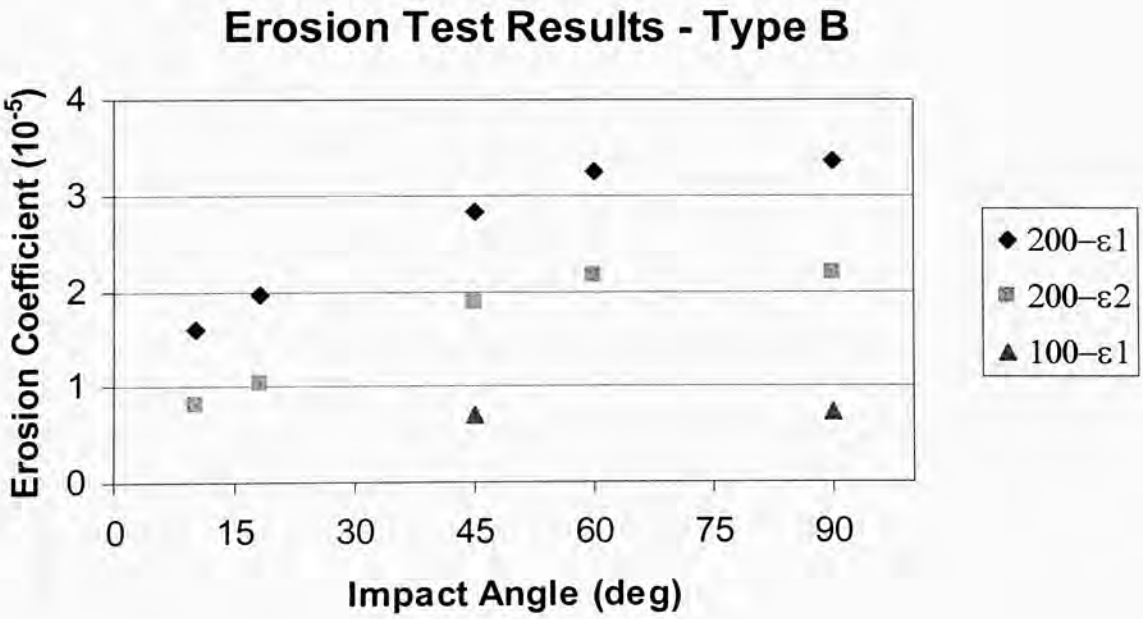

Figure 14. Type B material erosion results plotted vs. impact angle.

Table 6. Test results for the Type C material erosion tests.

200 (ft/sec)			1st Test			2nd Test			3rd Test
Impact Angle	Sample Mass Loss (g)	SiC Mass (g)	ε_1	Sample Mass Loss (g)	SiC Mass (g)	ε_2	Sample Mass Loss (g)	SiC Mass (g)	ε_3
10	0.0652	2267.95	2.8748E-05	0.0526	2267.95	2.3193E-05			
18	0.0893	2267.95	3.9375E-05	0.0749	2267.95	3.3025E-05			
45	0.1931	3171.3	6.0890E-05	0.1693	3171.30	5.3385E-05			
45	0.0869	2267.95	3.8317E-05	0.0755	2267.95	3.3290E-05			
45	0.1341	2267.95	5.9128E-05						
45	0.1523	2267.95	6.7153E-05	0.1228	2267.95	5.4146E-05			
60	0.2131	3171.3	6.7196E-05	0.1885	3171.30	5.9439E-05			
90	0.1784	2267.95	7.8661E-05	0.1579	2267.95	6.9622E-05	0.1584	2267.95	6.9843E-05
90	0.1864	2267.95	8.2189E-05	0.1592	2267.95	7.0196E-05			

100 (ft/sec)						
Impact Angle	Sample Mass Loss (g)	SiC Mass (g)	ε_1	Sample Mass Loss (g)	SiC Mass (g)	ε_2
45	0.039	2267.95	1.7196E-05	0.0249	2267.95	1.0979E-05
90	0.0368	2267.95	1.6226E-05	0.0252	2267.95	1.1111E-05

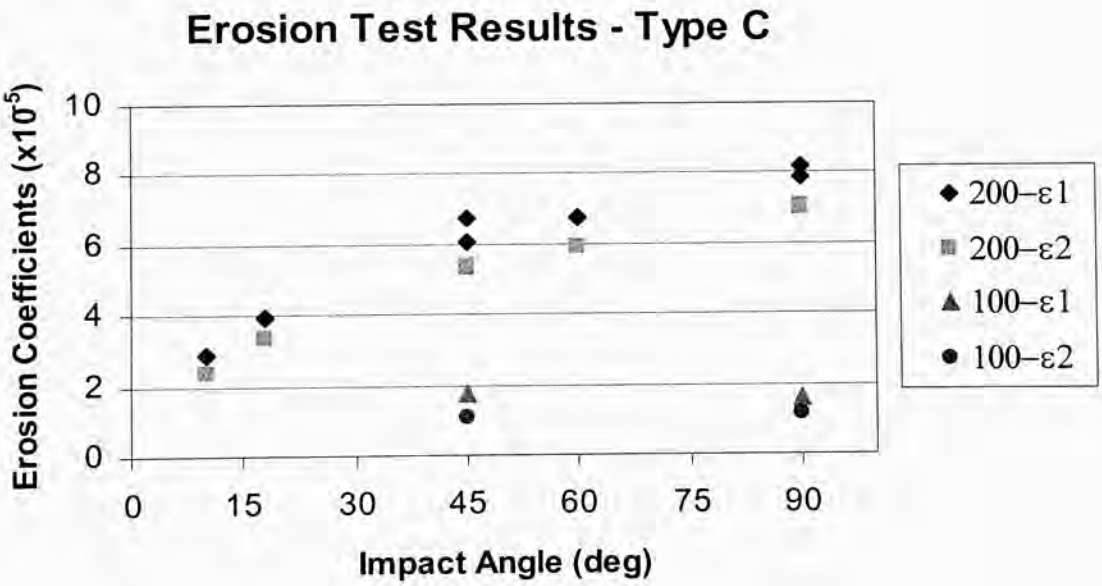

Figure 15. Type C material erosion results plotted vs. impact angle.

Table 7. Test results for the Type D material erosion tests.

200 (ft/sec)			1st Test			2nd Test
Impact Angle	Sample Mass Loss (g)	SiC Mass (g)	ε_1	Sample Mass Loss (g)	SiC Mass (g)	ε_2
10	0.0920	2268.0	4.0564E-05	0.0896	2268.0	3.9506E-05
18	0.1162	2268.0	5.1235E-05	0.1163	2268.0	5.1279E-05
45	0.1921	2268.0	8.4700E-05	0.1687	2268.0	7.4383E-05
45	0.1822	2268.0	8.0335E-05			
45	0.1849	2268.0	8.1526E-05	0.1568	2268.0	6.9136E-05
60	0.2099	2268.0	9.2549E-05	0.1899	2268.0	8.3730E-05
90	0.2388	2268.0	1.0529E-04	0.2203	2268.0	9.7134E-05
90	0.2525	2268.0	1.1133E-04	0.2347	2268.0	1.0348E-04
100 (ft/sec)						
Impact Angle	Sample Mass Loss (g)	SiC Mass (g)	ε_1	Sample Mass Loss (g)	SiC Mass (g)	ε_2
45	0.0524	2268.0	2.3104E-05	0.0417	2268.0	1.8386E-05
90	0.0624	2268.0	2.7513E-05	0.0520	2268.0	2.2928E-05
70 (ft/sec)	Sample Mass Loss (g)	SiC Mass (g)	ε_1			
45	0.0408	3628.7	1.124E-05			

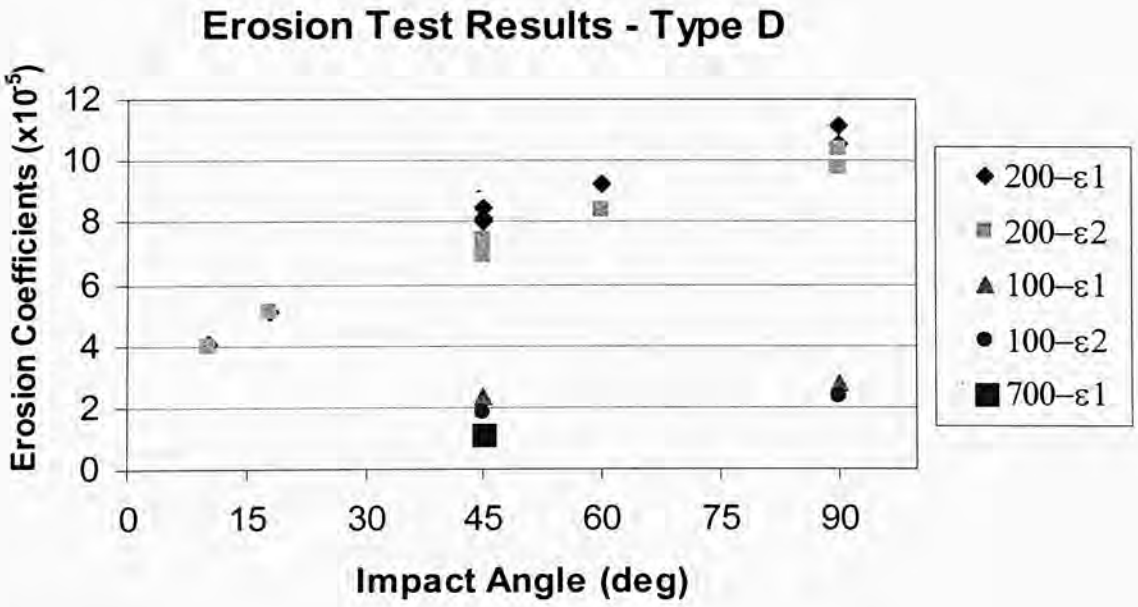

Figure 16. Type D material erosion results plotted vs. impact angle.

Table 8. Test results for the Type E material erosion tests.

200 (ft/sec)			1st Test			2nd Test
Impact Angle	Sample Mass Loss (g)	SiC Mass (g)	ε_1	Sample Mass Loss (g)	SiC Mass (g)	ε_2
10	0.0223	2268.0	9.8325E-06	0.0122	2268.0	5.3792E-06
18	0.0294	2268.0	1.2963E-05	0.0172	2268.0	7.5838E-06
45	0.0476	2268.0	2.0988E-05	0.0333	2268.0	1.4683E-05
45	0.0472	2268.0	2.0811E-05	0.0314	2268.0	1.3845E-05
60	0.0500	2268.0	2.2046E-05	0.0367	2268.0	1.6182E-05
90	0.0572	2268.0	2.5220E-05	0.0422	2268.0	1.8607E-05

100 (ft/sec)			
Impact Angle	Sample Mass Loss (g)	SiC Mass (g)	ε_1
45	0.0138	3628.7	3.8030E-06
90	0.0196	3628.7	5.4014E-06

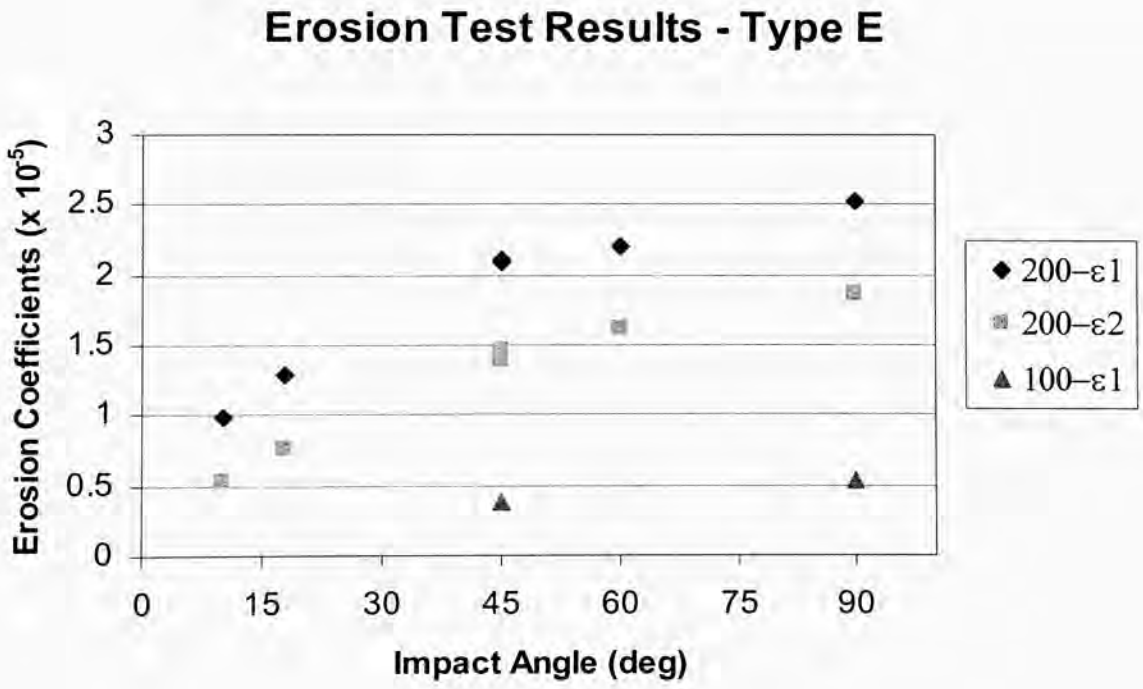

Figure 17. Type E material erosion results plotted vs. impact angle.

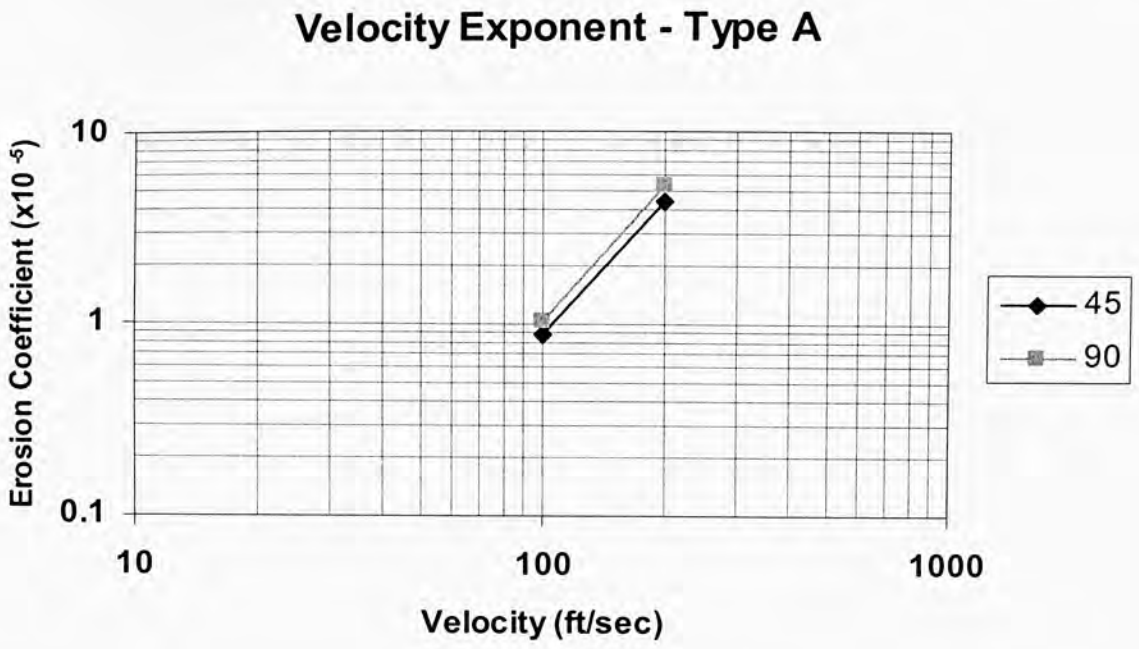

Figure 18. Log/log plot of corresponding data points for Type A material.

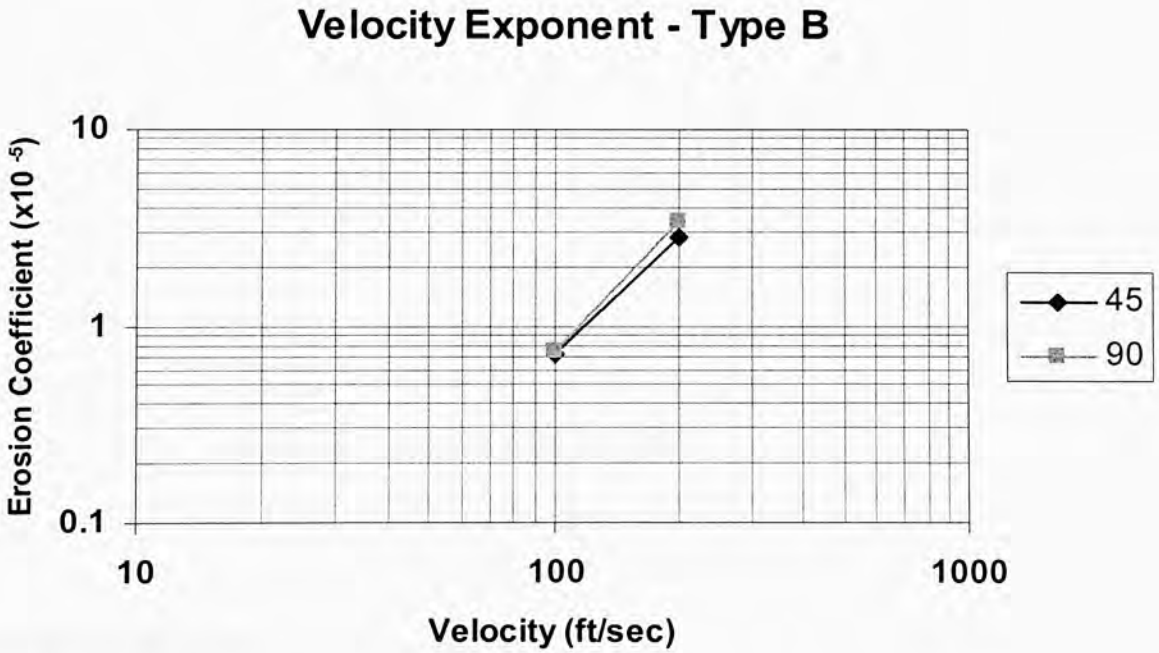

Figure 19. Log/log plot of corresponding data for Type B material.

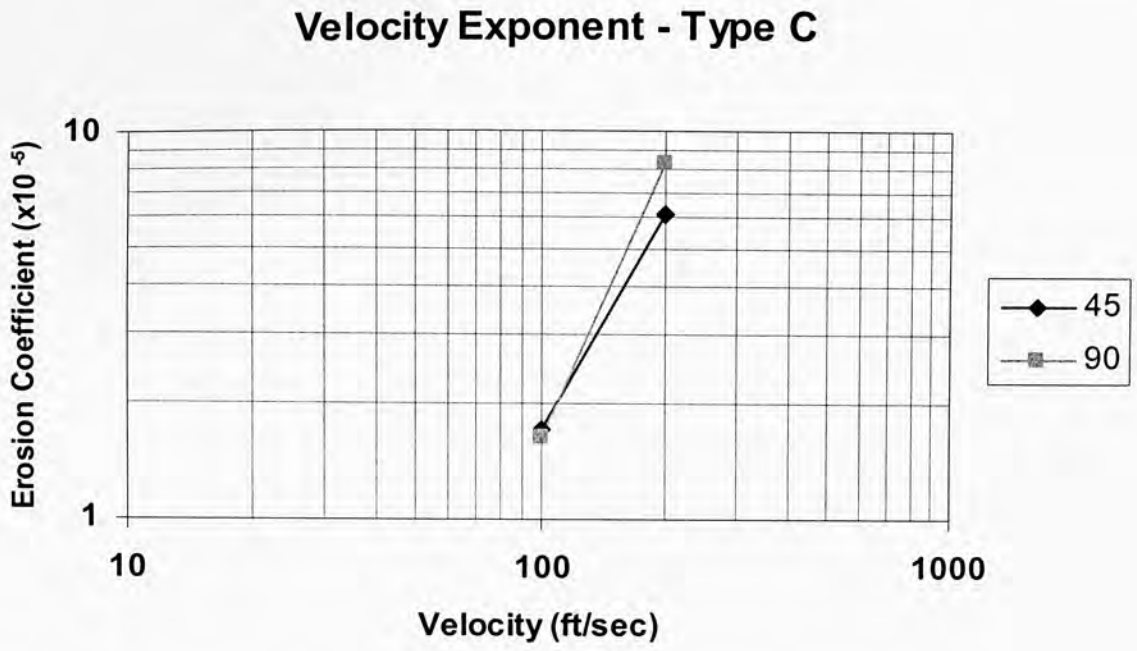

Figure 20. Log/log plot of corresponding data for Type C material.

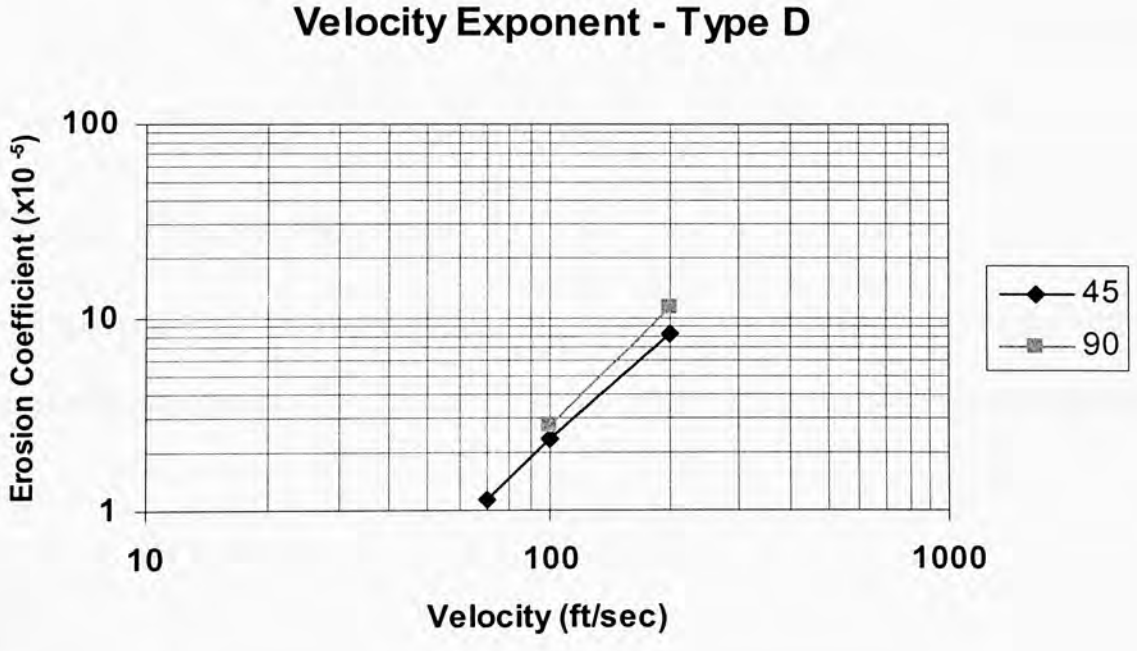

Figure 21. Log/log plot of corresponding data for Type D material.

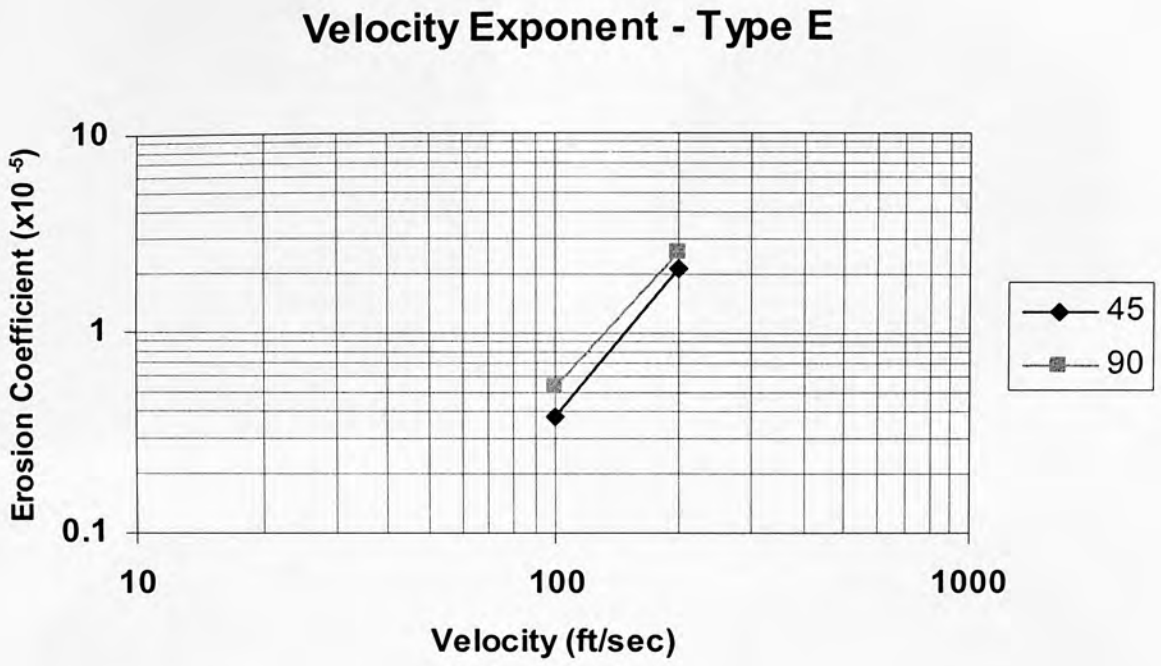

Figure 22. Log/log plot of corresponding data for Type E material.

tests. Velocity exponents were computed from the straight line plots. The calculations are given in Chapter 5.

4.3 Material Sample Photographs

Figures 23 – 27 are photographs of the material samples after each of the tests. These samples are grouped by the particle impingement angle that was used during the tests.

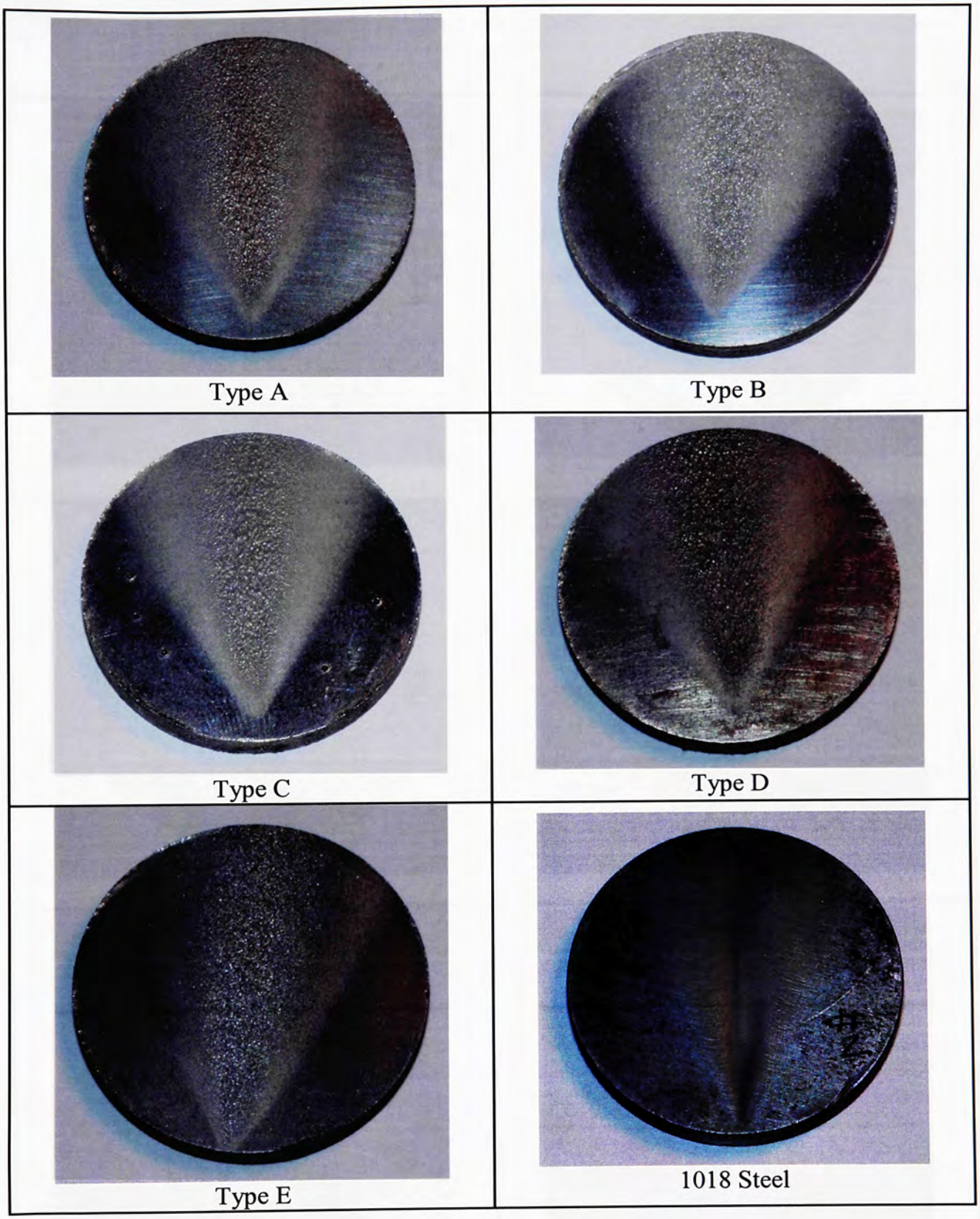

Figure 23. 10° erosion samples.

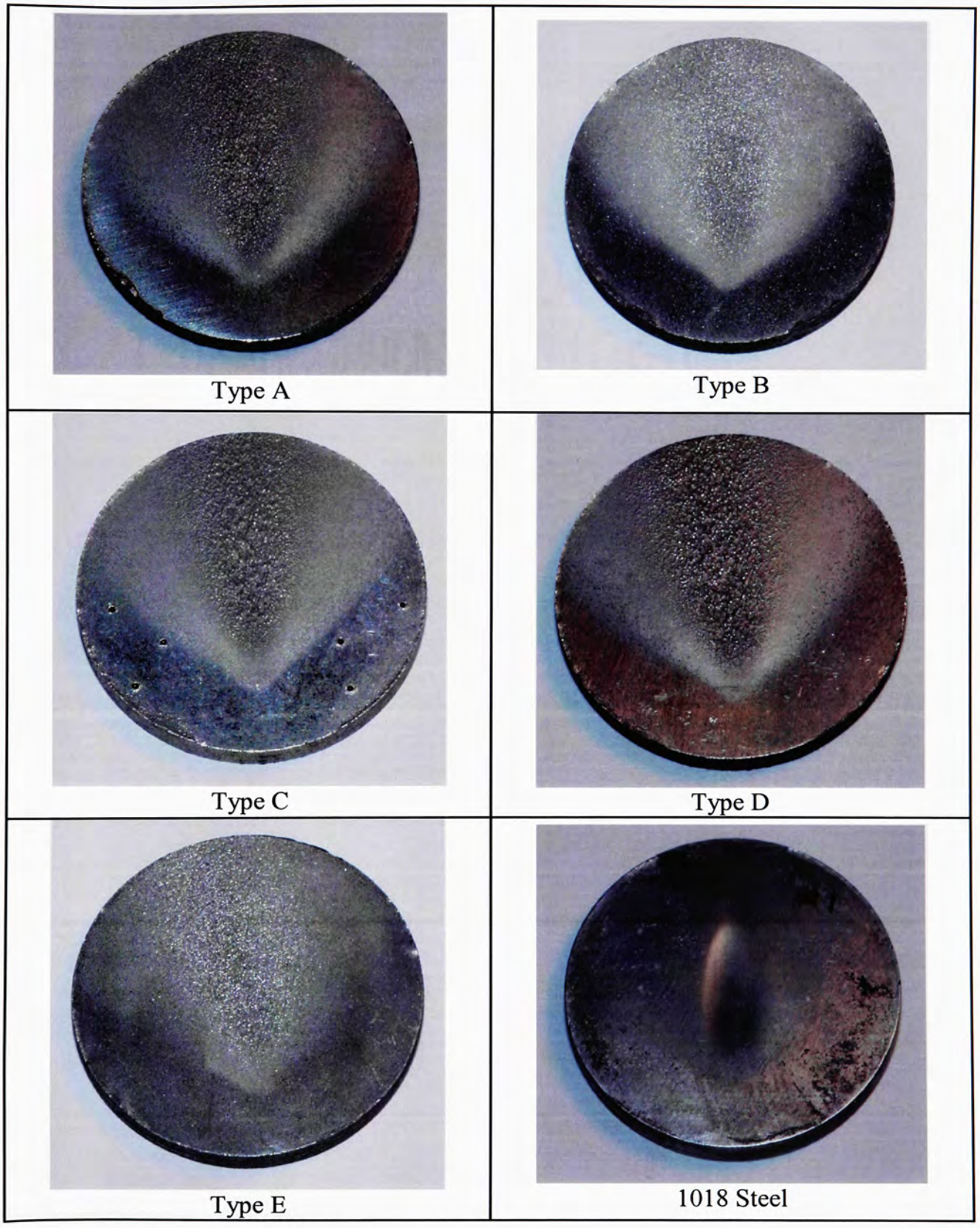

Figure 24. 18° erosion samples.

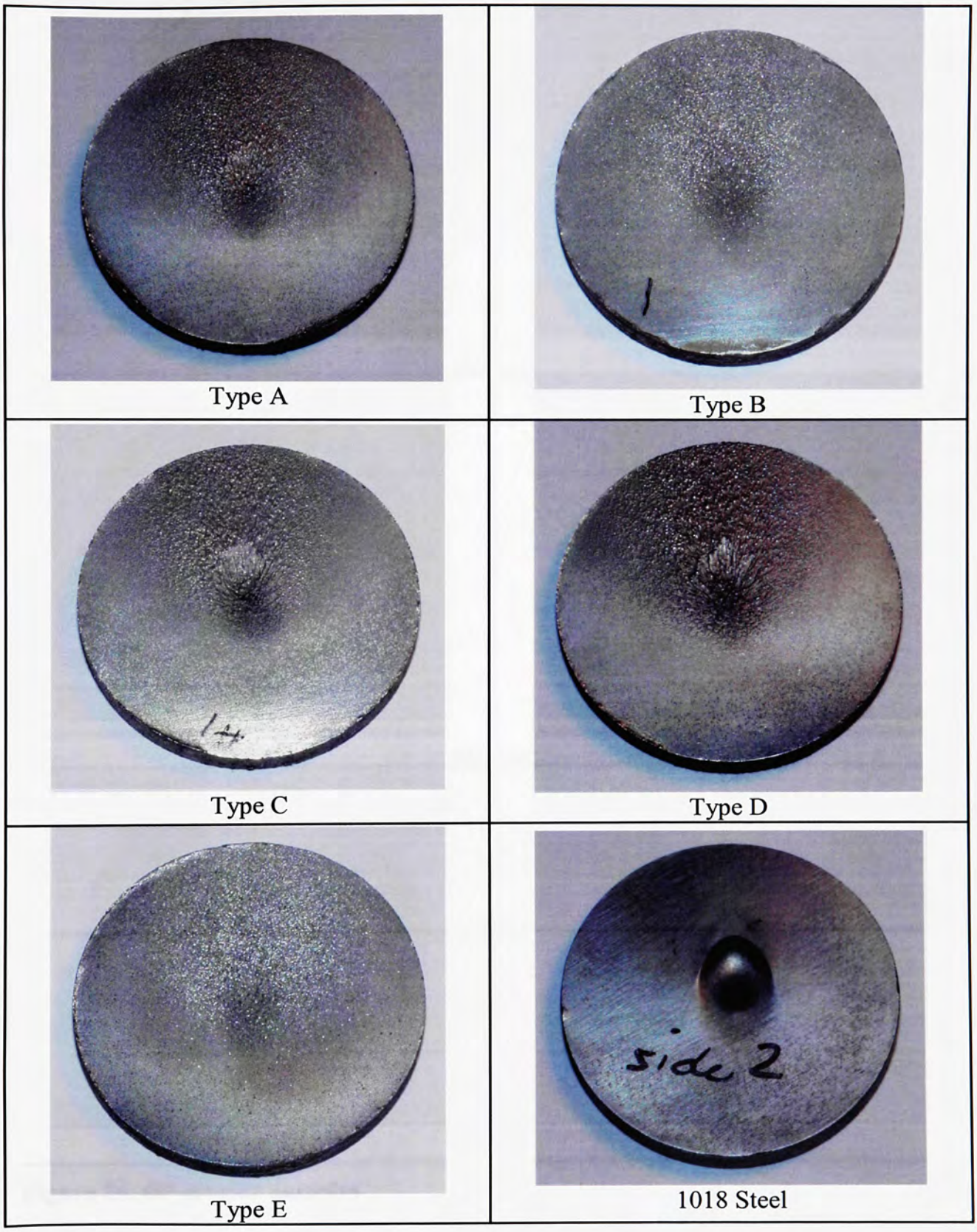

Figure 25. 45° erosion samples.

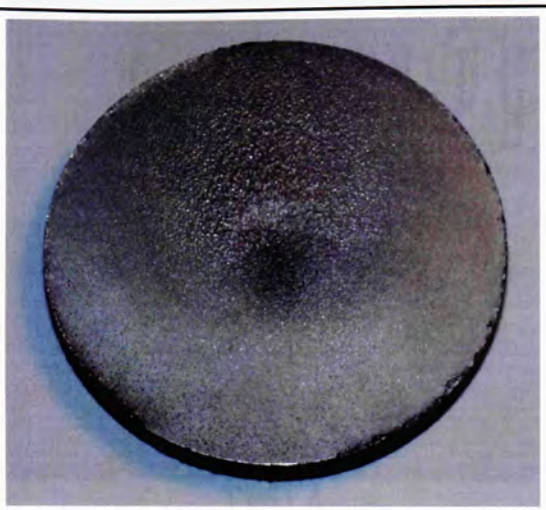

Type A

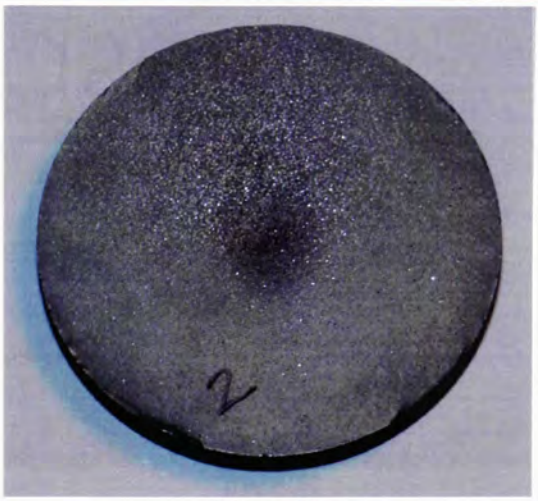

Type B

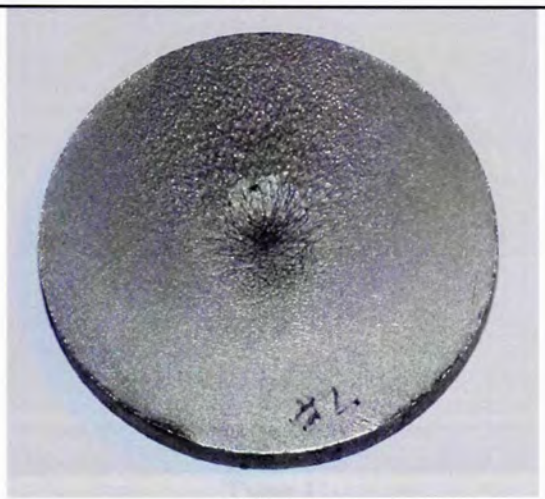

Type C

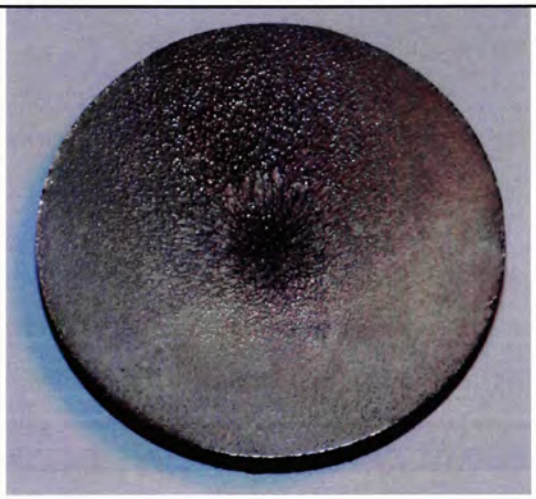

Type D

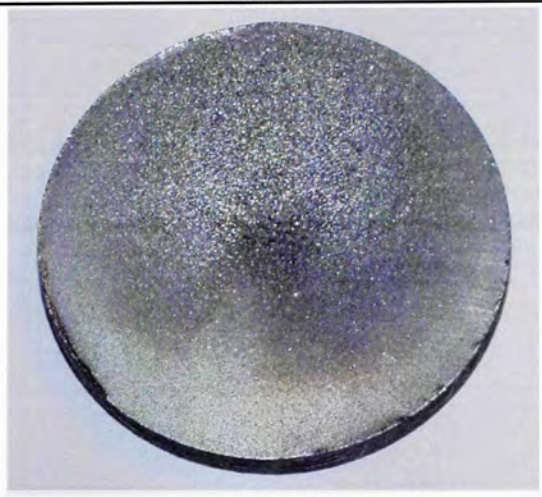

Type E

No test at 60°

1018 Steel

Figure 26. 60° erosion samples.

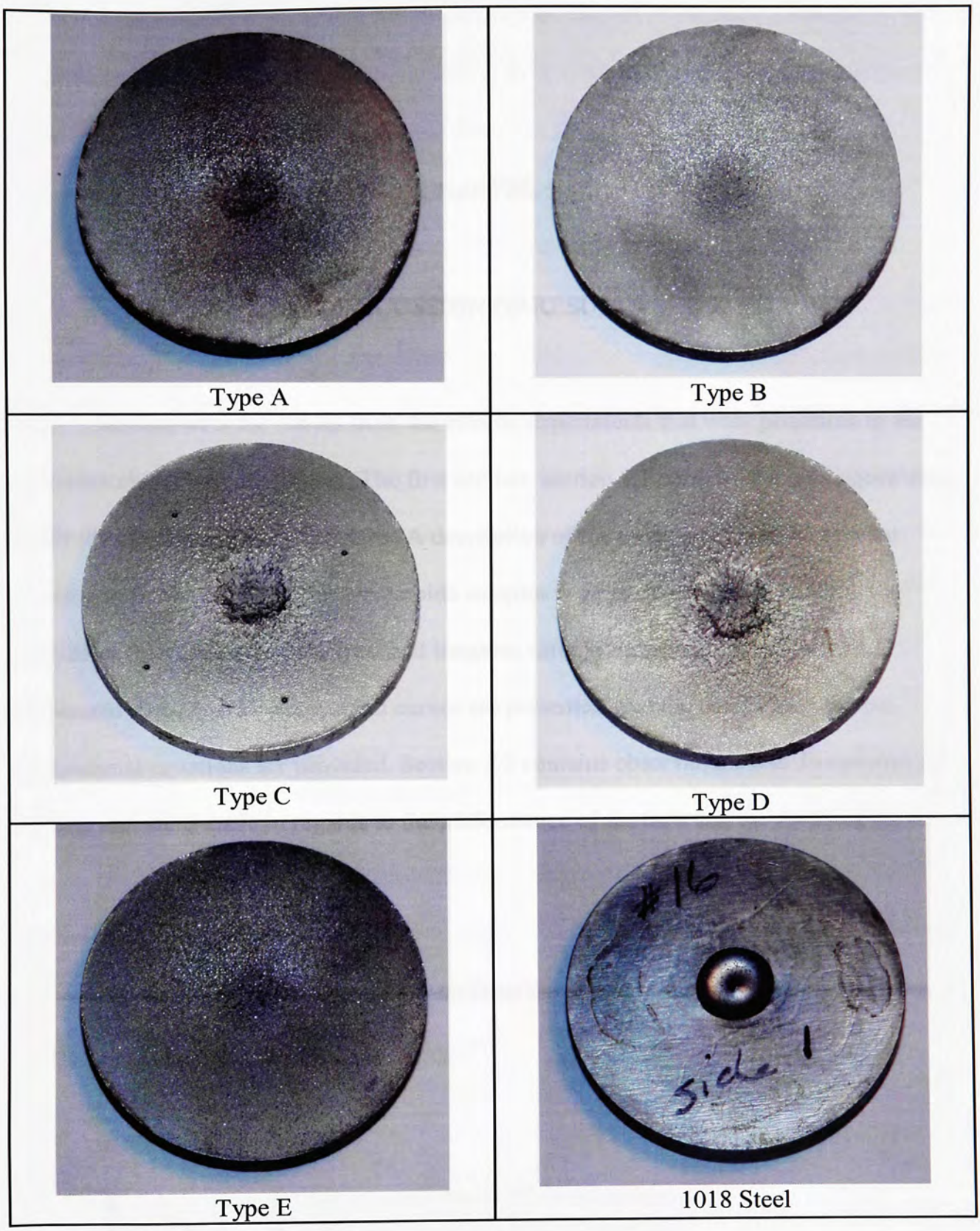

Figure 27. 90° erosion samples.

CHAPTER 5

DISCUSSION OF RESULTS

In Chapter 5 the results from the erosion experiments that were presented in the previous chapter are discussed. The first section, section 5.1 contains the techniques used to fit the experimental erosion data. A description of the procedures used to develop equations for the various tungsten carbide samples is given. Section 5.2 includes the results of the curve fits of the steel and tungsten carbide materials. Graphs of the measured data, fit with polynomial curves are presented, and the coefficients for the polynomial equations are provided. Section 5.3 contains observations and discussions of results that were made in regards to the performance of the tests and the resulting data.

5.1 Curve Fit Calculations

The particle erosion rate data were fit to the general equation given by Humphrey (12):

$$\varepsilon = ZV^n F(\theta) \qquad (13)$$

Z	=	constant, specific to the material specimen
V	=	particle velocity relative to the specimen
n	=	velocity exponent
$F(\theta)$	=	a polynomial function of the particle impingement angle θ

This relation neglects particle size effects as they were not included in the experiments. The experimental data obtained for various particle impingement angles was fit to 2nd and 3rd degree polynomials forced to zero.

5.1.1 Fitted Erosion Data with Respect to Particulate Impingement Angle

The functional relation for the particle impingement angle effects on erosion rate was analyzed using the experimental data obtained for impingement angles of 18, 45, 60, and 90°. Measurements made at lower impingement angles could not be used because the spread of the jet imposed an "apparent" impingement angle that, when added to that based on the angle made by the jet axis on the specimen face, significantly increased the average angle of particle impact. The data for each specimen material type were fitted using linear least square techniques and is plotted with the equations in the following pages. These figures show a comparison between the experimental data and the fitted curves. Also in Eq. 13 is the coefficient Z, which is a fitted constant that is distinct for the various particle and specimen properties.

The data are grouped in subsections that represent the different types of material samples. The steel samples are presented first, followed by the different tungsten carbide samples, Types A - E. A summary chart is included in section 5.2.7 comparing the different erosion rate curves on the same chart.

5.1.2 Velocity Exponent Calculations

The velocity exponent dictates the extent of the influence of particle velocity on the erosion rate. When the erosion rate is plotted against particle velocity on log/log

coordinates the result is generally linear. See Figures 18-22. The velocity exponent is calculated by measuring the slope of the straight line that connects the erosion rates values for experiments conducted at the same impact angles and different velocities. Two sets of data were used for each velocity exponent calculation, one obtained at 45° and the other at 90°. The results from these two data sets were averaged to obtain the velocity exponent for each material.

The velocity exponent for each material was found to be unique. The resulting velocity exponents for all the materials are listed in Table 9.

5.2 Results for Material Test Samples

The following sections contain the original measured test data with fitted curves through the data. There is also an equation given for each test material, that represents the fitted curve in terms of the variables, velocity and impact angle.

5.2.1 1018 Steel Samples

Equation 14 is the fitted polynomial equation that describes the relationships of the impact angle and velocity to the measured erosion coefficients for the 1018 steel samples. Figure 28 is a graph of the experimentally determined erosion coefficients with

Table 9. Velocity exponents for the Steel and Tungsten Carbide Samples, Types A-E.

	Steel	Type A	Type B	Type C	Type D	Type E
Velocity Exponent	2.0	1.70	0.45	1.40	2.00	1.25

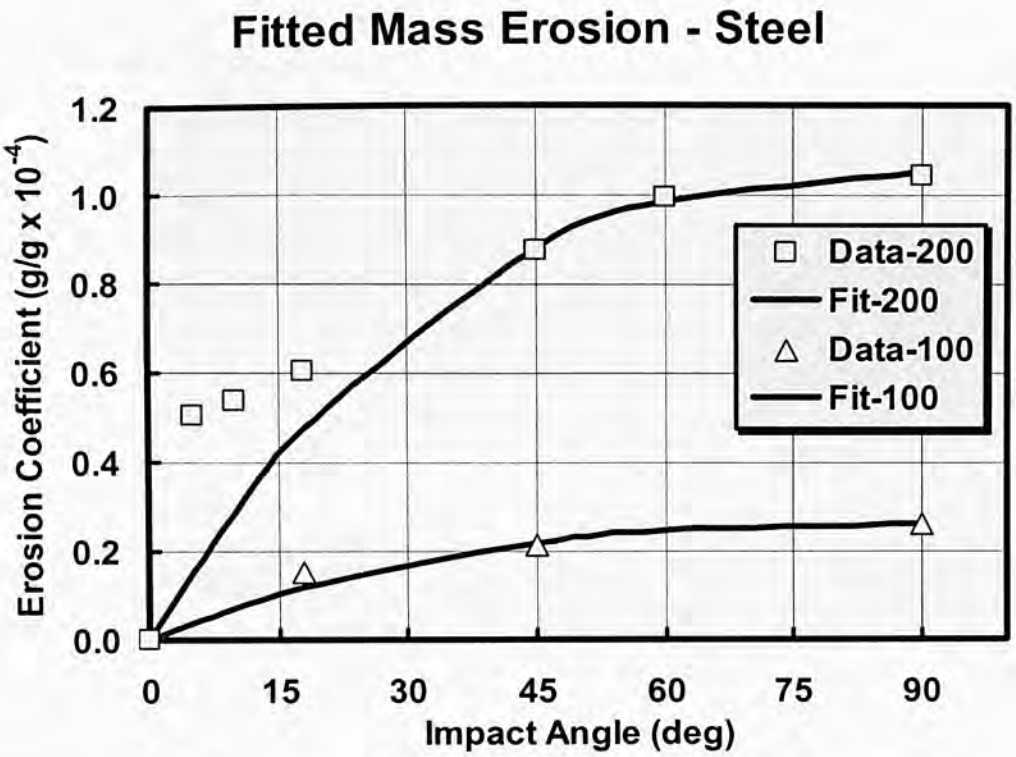

Figure 28. Erosion coefficient data with fitted curves for steel.

the resultant curves plotted through the data. The two curves in the graph represent results for the different particle impact velocities. The particle angle data are fitted using a third degree polynomial.

$$\varepsilon = (2.52\text{E}-09)V^{2.0}(3.16159\cdot 10^{-02}x - 3.19575\cdot 10^{-04}x^2 + 1.08111\cdot 10^{-06}x^3) \qquad (14)$$

5.2.2 Tungsten Carbide Type A Samples

Equation 15 is the resulting fitted equation that describes the effect of the particle impact angle and velocity to the erosion coefficient for the Type A tungsten carbide samples. Figure 29 compares the fitted curve with the experimental data.

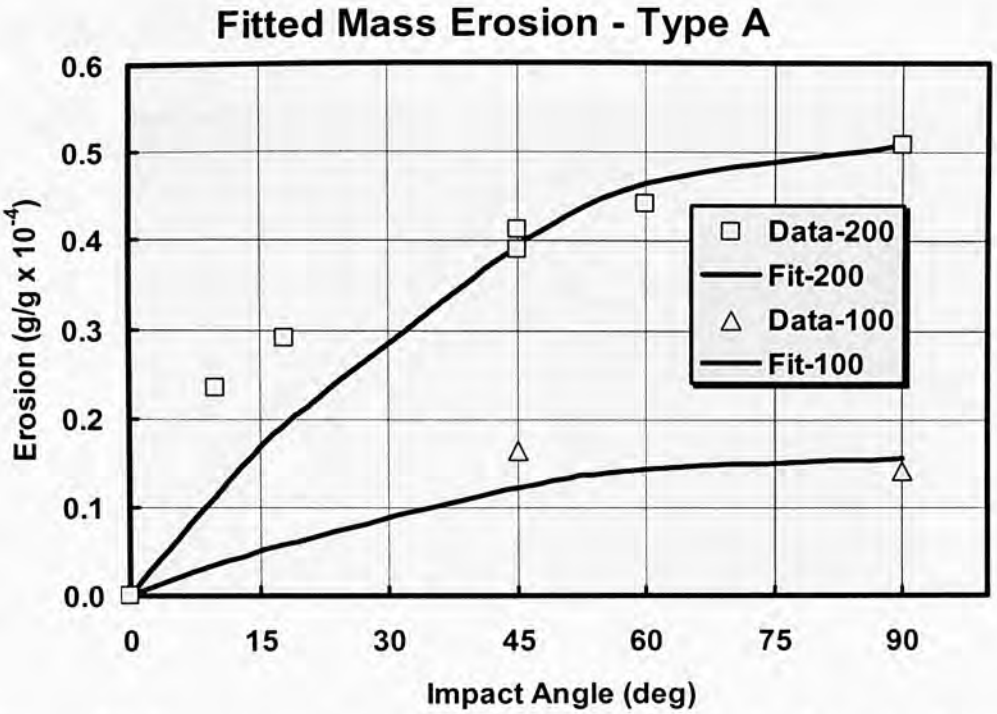

Figure 29. Erosion coefficient data with fitted curves for the Type A samples.

$$\varepsilon = (1.23E-08)V^{1.7}(1.1865\cdot 10^{-02}x - 6.9553\cdot 10^{-05}x^2) \tag{15}$$

5.2.3 Tungsten Carbide Type B Samples

Equation 16 is the fitted equation describing the effect of particle impact angle and velocity on the erosion coefficient for the Type B tungsten carbide samples. The fitted curve is plotted against the experimental data in Figure 30.

$$\varepsilon = (9.20E-06)V^{.45}(7.3735\cdot 10^{-03}x - 4.7805\cdot 10^{-05}x^2) \tag{16}$$

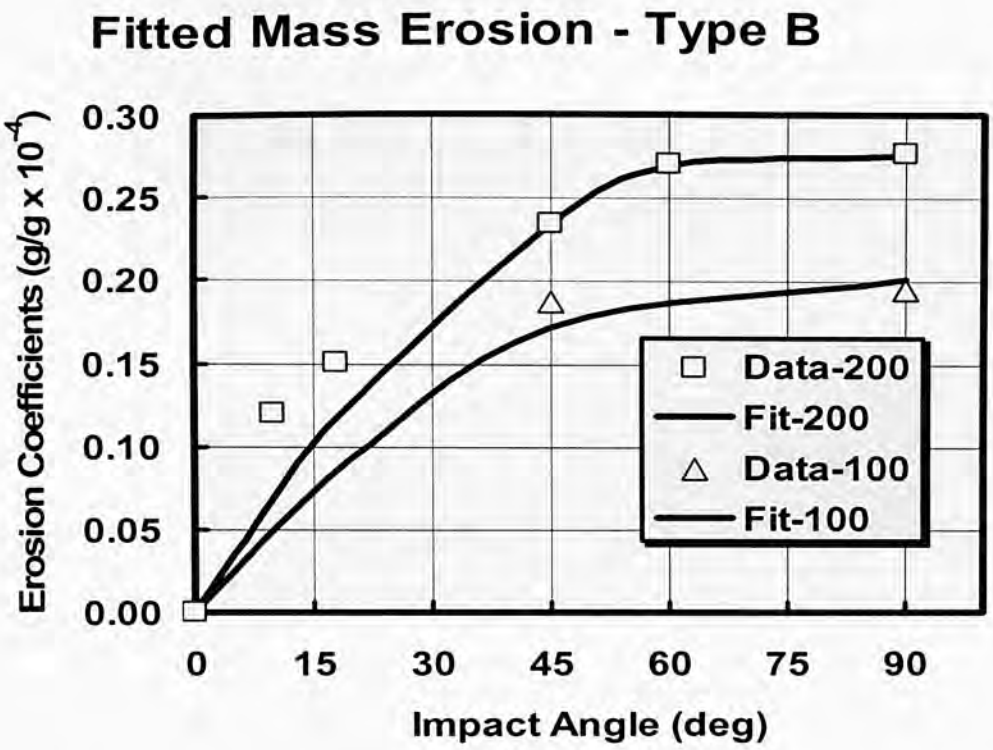

Figure 30. Erosion coefficient data with fitted curves for the Type B samples.

5.2.4 Tungsten Carbide Type C Samples

Equation 17 is the resulting equation describing the relationship between particle impact angle and velocity and the erosion coefficient for the Type C tungsten carbide samples. Figure 31 is a graph of the experimental data plotted with the resultant curve.

$$\varepsilon = (6.00E-08)V^{1.4}(1.4836\cdot 10^{-02}x + 4.50839\cdot 10^{-05}x^2 - 1.3011\cdot 10^{-06}x^3) \qquad (17)$$

5.2.5 Tungsten Carbide Type D Samples

Equation 18 is the fitted polynomial equation that describes the relationship between the particle impact angle and velocity to the erosion coefficient for the Type D

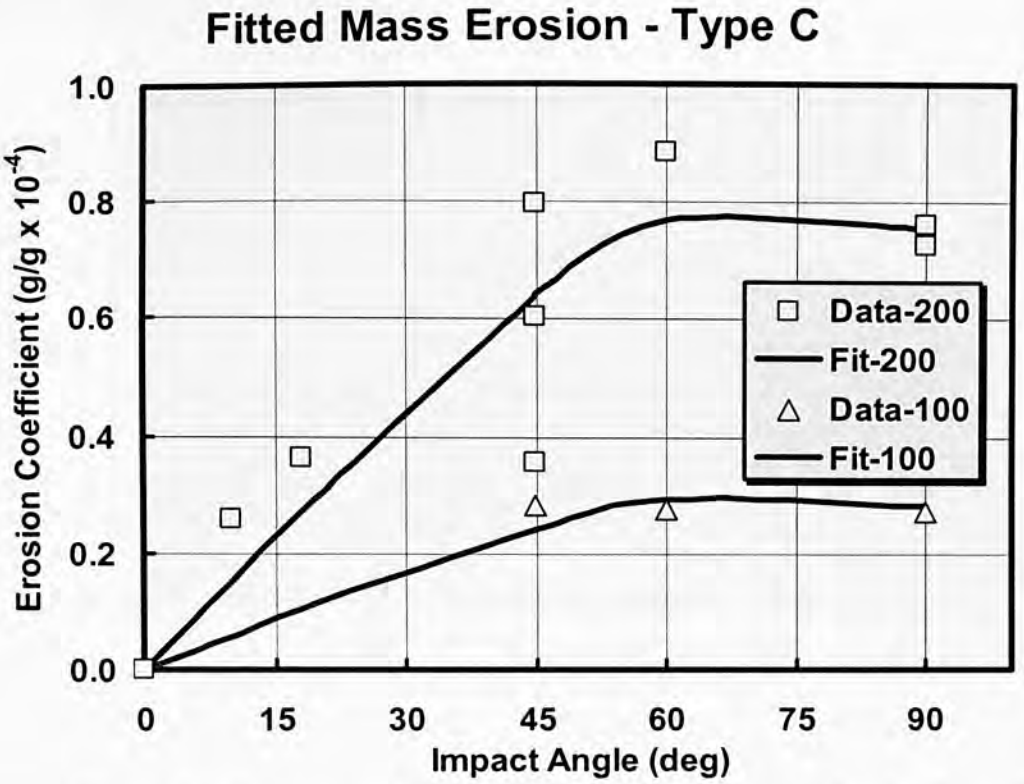

Figure 31. Erosion coefficient data with fitted curves for the Type C samples.

tungsten carbide samples. Figure 32 shows the fitted curve plotted against the experimental data.

$$\varepsilon = (2.50E-09)V^{2.0}(2.2785\cdot 10^{-02}x - 1.2882\cdot 10^{-04}x^2) \quad (18)$$

5.2.6 Tungsten Carbide Type E Samples

Equation19 is the fitted polynomial equation describing the relationship between the particle impact angle and velocity and the erosion coefficient for the Type E tungsten carbide samples. The fitted curve is plotted against the experimental data in Figure 33.

$$\varepsilon = (1.33E-07)V^{1.25}(5.2162\cdot 10^{-03}x - 3.1163\cdot 10^{-05}x^2) \quad (19)$$

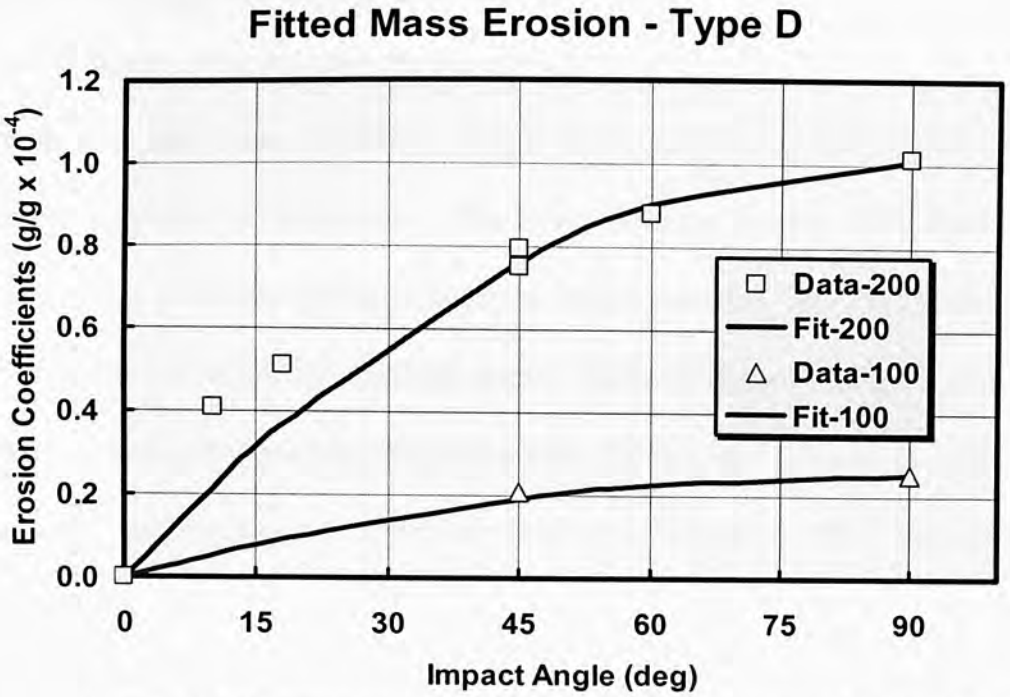

Figure 32. Erosion coefficient data with fitted curves for the Type D samples.

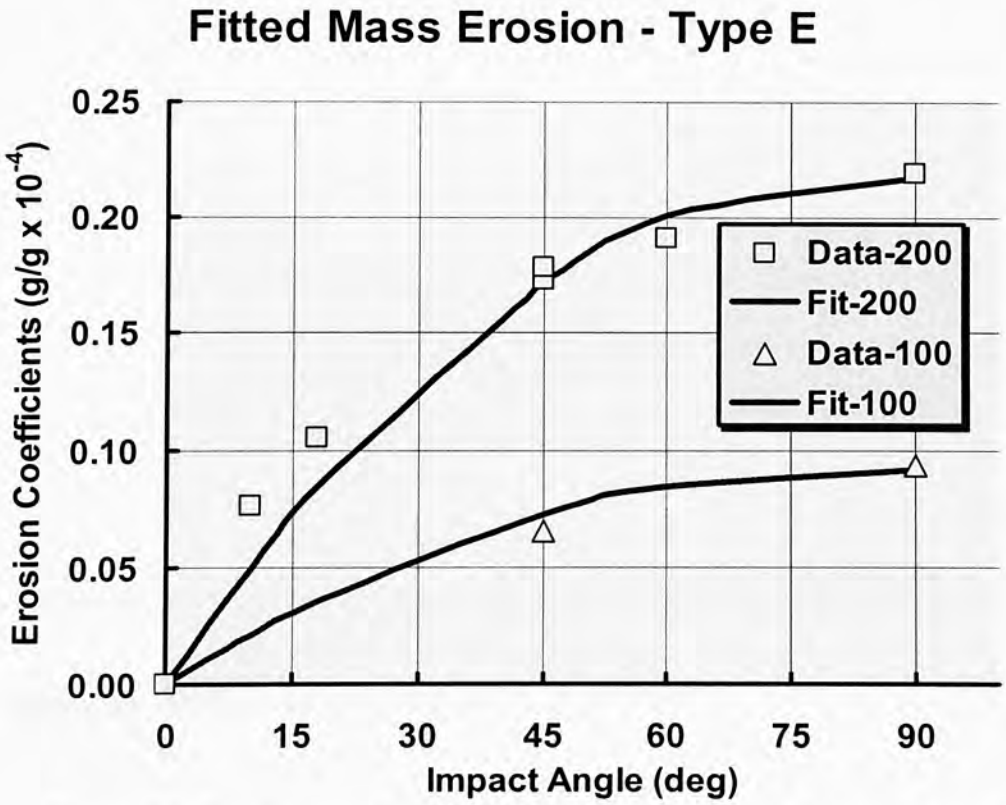

Figure 33. Erosion coefficient data with fitted curves for the Type E samples.

5.2.7 Summary Comparison for All of the Material Types

Figure 34 compares the resulting fitted curves at 200 ft/sec obtained for all the material types. These results show that the rate of erosion increases with higher particle impact angle for all specimens. The curves indicate that the 1018 Steel is most susceptible to erosion while Tungsten Carbide material Type E exhibits the highest erosion resistance of the materials tested. Material Type D exhibits erosion characteristics that are very similar to that of 1018 steel. All of the materials tested indicate a decreasing rate of erosion with high impingement angle, as the impact angle approached 90°, as shown by a flattening of the curves. Only Type C showed a decrease in the actual erosion rate at 90°.

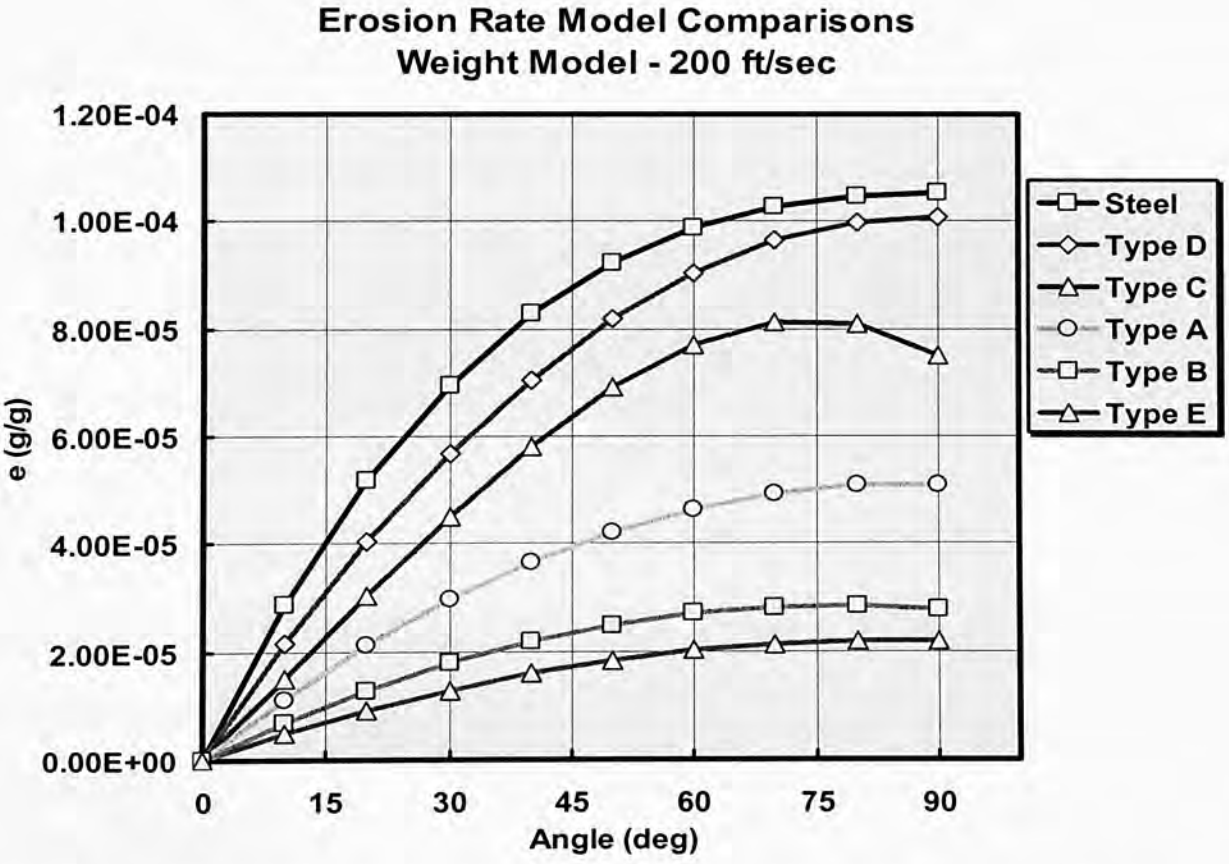

Figure 34. A summary and comparison between the 200 ft/sec resulting equations.

5.3 Observations and Discussion of Results

This section contains a discussion of observations made during the experiments.

5.3.1 Process of Erosion

The erosion rate results that have been presented represent the rate at which material is removed from the tungsten carbide samples when impacted by a jet blast of silicon carbide particles. When tungsten carbide samples were tested, the resulting erosion was found to occur as a result of a specific mechanism.

Particle erosion of tungsten carbide begins with the removal of the binder material that holds the individual carbide particles in place. The removal of the binder material weakens the bonds between the binder and carbide particles so that subsequent impacts of the erodent tend to dislodge the carbide particles from the surface.

Examples of the erosion cavity created in tungsten carbide are shown in Figures 35 – 36. These are photographs of the cavity created by impacts of silicon carbide particles impinging at 90°. The rough surface texture of the cavity is primarily due to the remaining exposed carbides. Figure 35 shows flow from the vertical impingement scouring paths that migrate radially outward from the impingement center.

Individual carbides in the impact cavity are seen in Figure 36. This figure illustrates actual carbide particles that have been exposed through erosion. Carbide particles like these are continuously exposed and removed as the binding material is lost due to the process of erosion.

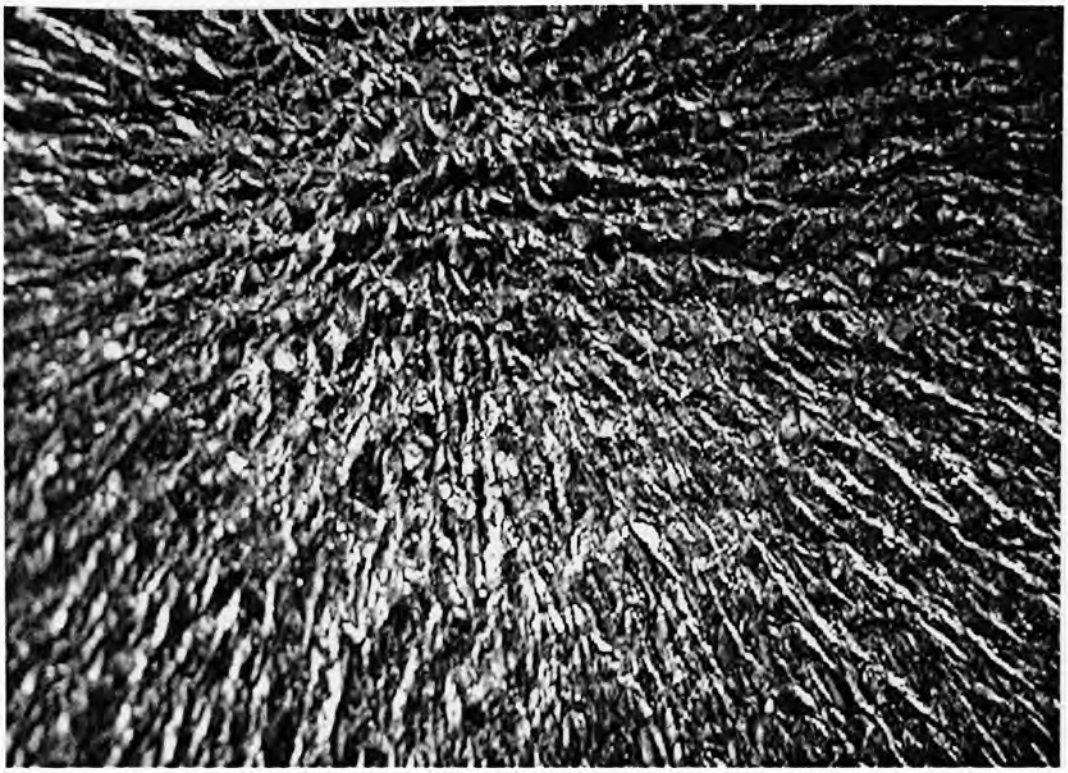

Figure 35. Flow paths created by the impacting silicon carbide particles throughout the impact cavity.

Figure 36. Photograph of the individual carbides remaining in the impact cavity.

5.3.2 Steady State Erosion

The rate of erosion of the tungsten carbide materials was generally measured over two consecutive tests. In every test, the measured erosion rate was higher for the first test than for the second test (see Figures 12 – 17). After the initial high rate, the rate of erosion was observed to reach a steady state value on subsequent tests. The reason for this is that at the onset of the erosion process, the binder material surrounding the tungsten carbide particles is more exposed, or relatively flush with the surface of the tungsten carbide particles. The relatively ductile binder is rapidly removed at this stage, allowing the tungsten carbide to be dislodged at a higher rate. Once the cavity begins to form, the more easily accessible binder at the surface has been removed and the remaining binder is less exposed to the erodent. At this stage the erosion rate stabilizes and approaches a pseudo-steady state.

5.3.3 Cavity Effect on the Erosion Rate

As the material is removed a small cavity is created in the sample. The formation of this cavity effectively changes the angle at which the impacting particles make contact with the target sample. This also influences the direction that the particles rebound off of the sample. Any change to the impact angle then necessarily changes the measured erosion rate as seen in the experiments. In addition, particles rebounding within the cavity, if allowed to gain significant size, could create a buffer zone where particle to particle interactions would essentially shield the sample and reduce the rate of erosion. In the above experiments, care was taken to insure that the eroded cavity remained small.

5.3.4 Low Angle Particle Impact Tests (5° and 10°)

On tests conducted using shallow particle impact angles, such as 5 and 10°, it was observed that the fluid stream would actually come in contact with the side of the sample. The fluid stream that impacts the side of the samples strikes the sample at an angle of 80 to 90°. The result of this impact is that the erosion forms gouges that pass through the side and across the face of the sample. This phenomenon is illustrated in the pictures of the tungsten carbide samples at the end of Chapter 4 (see Figure 22).

This shallow angle causes the impact region on the samples to cover a much larger area at this shallow angle than when the impact angle is steeper.

In addition, as the turbulent jet stream leaves the nozzle, it theoretically spreads at an angle of approximately 7-1/2°. When added to the actual impact angle, as determined by the angle between the jet axis and the specimen, the actual particle impingement angle experienced by the test sample was significantly higher than that imposed, resulting in higher erosion rates.

5.3.5 Determination of the Coefficient of Restitution

It was of interest to measure the direction that the erodent particles were reflected away from the specimen surface, known as the coefficient of restitution. To determine the direction taken by the silicon carbide particles once they leave the specimen surface strips of aluminum were placed along the outer wall of the test vessel. As the particles were rebound from the target samples they would strike the aluminum strips leaving an etch mark on the surface. The etch mark was then used to measure the refraction angle.

The measured refraction angle, in every case, very nearly matched the angle at which the samples were placed in the sample holder. This indicates that the particles remain entrained in the slurry flow and follow the flow path away from the sample holder after impingement on the tungsten carbide samples.

CHAPTER 6

SUMMARY AND CONCLUSION

Chapter 6 contains a summary of the experiment and provides a conclusion to this research. Included in this chapter the thesis statement is repeated, along with a summary of the work completed and the results, conclusions drawn from the research, and a recommendation for future work on this area of study.

6.1 Thesis Statement

The objective of this study is to experimentally determine the relative slurry erosion rates for five tungsten carbide compositions. The functional relationship between the rate of erosion, the relative solid particle velocity and angle of particle impingement are established. Algebraic equations are provided that define the erosion rate for the five compositions of tungsten carbide plus the sample of mild steel in terms of the velocity and impingement angle of the slurry flow.

6.2 Summary of Work and Results

The testing for this thesis was accomplished by a jet impact of abrasive particles in a slurry flow. The slurry flow was forced through a nozzle and directed at material

samples of the six material samples examined in this study. The erosion was caused by silicon carbide particles contained within the slurry. A specially designed pump was used to force the abrasive silicon carbide particles into the flow stream.

For each of the material samples, tests were conducted at different impact angles and velocities to establish the pattern of erosion behavior for each of the different material samples.

The erosion rate was measured by establishing the ratio of mass loss on the material samples divided by the mass of impacting erodent particles. The erosion rate was then plotted on charts versus the impact angle and impact velocity. Algebraic equations were then fitted to the experimental data.

The experimental results showed a wide variety of erosion rates for the different material samples. A comparison of the results on the same chart can be seen in Figure 34, in Chapter 5. The tungsten carbide sample that had the worst erosion resistance had results that differed only slightly from the results of the mild steel sample, whereas the most erosion resistant tungsten carbide sample had results that were almost an order of magnitude better than this worst case sample.

6.3 Conclusions

One of the most interesting conclusions from this research is found in the shape of the resulting erosion curves. Levy (2) in his slurry erosion research developed a curve that had a bimodal representation. This bimodal curve had a local maximum at approximately 45°, with a local minimum at approximately 60°, and the maximum rate occurring at 90° (see Figure 4 in Chapter 2). In this research, the erosion rate curves

contained values that continued to increase from 0 to 90° (see Figures 28-33 in Chapter 5).

It was not possible to measure the erosion rate at all of the impact angles from 0 to 90° due to time and budget constraints, but specific angles were selected to check for a correlation between these resulting curves and Levy's.

One possible explanation for the different shapes of the curves is that Levy's curves were developed at a much slower velocity (13 m/s) than was used in these experiments (100 - 200 ft/sec). At the slower velocity, the particles would have a harder time penetrating the fluid boundary layer of the samples, which would reduce the severity of the particle impact.

An additional explanation could be the erosive particle density in the fluid flow used in Levy's experiments. The weight percentage concentration of abrasive particles in Levy's slurry was higher and therefore had the potential for more particle to particle interaction which would decrease the erosive potential of the particles. This could possibly be explanation as to why there are two different curve shapes for slurry erosion.

The results from this study will also be beneficial to the manufacturers of drill bits, or other products that are manufactured with tungsten carbide that are exposed to erosive fluid flows. The results show that the best way to reduce the erosion rate of tungsten carbide is to minimize the angle at which the erosive particles will make contact with the tungsten carbide. These results can be used to establish design rules for products that are manufactured with tungsten carbide to help predict the life expectancy under abrasive slurry flow.

6.4 Suggestions for Further Research

This research has examined a small, specific area of slurry erosion. There exist potentially large areas or topics for further research. These areas could include investigation into the initial erosion rate before reaching a steady state. As was shown with this research, the initial erosion rate test on each of the samples generally yielded a higher erosion rate as compared to the following subsequent tests on the same sample.

Another possible area is a more detailed examination of tungsten carbide with varying carbide grain size and cobalt content. This information could be used to establish rules for erosion rates on the basis of these two parameters. Along with this research could be the examination of the slurry erosion rate with the use of silicon carbide with particles of varying size. This effect has been studied with erosion in an air stream, but the effect could possibly be different with flow in a slurry stream.

APPENDIX

CALCULATIONS FOR THE NOZZLE FLOW COEFFICIENT

The nozzle flow coefficient (K), was computed from a simple experiment. The process involved measuring the time required to fill a container with a specified volume of water. These values were then placed into the generally recognized nozzle equation and the nozzle flow coefficient was calculated. The calculated results were averaged to yield a value of .97 that was used in the experiments.

The experimental data can be seen below.

Nozzle Area = 8.52×10^{-5} ft^2

Time (sec)	Volume (ft^3)	Flow Rate (ft^3/sec)	ΔP (psi)	K
30.1	0.678	0.022524917	510	0.961
29.45	0.658	0.022342954	490	0.972
31.04	0.682	0.021971649	480	0.966
39.55	0.668	0.016890013	280	0.972
39.5	0.667	0.016886076	280	0.972
75.08	0.677	0.009017048	80	0.971
74.97	0.674	0.008990263	80	0.968
73.29	0.659	0.008991677	80	0.968

REFERENCES

(1) Finnie, I., Erosion of Surfaces by Solid Particles, Wear, Vol. 3, 1960, p. 87-103.

(2) Levy, Alan V., 1995, *Solid Particle Erosion and Erosion-Corrosion of Materials*, ASM International, Materials Park, Ohio. (Chapter 8)

(3) Levy, A. V., Hickey, G., 1987, "Liquid-Solid Particle Slurry Erosion of Steels," Wear, Vol. 117, pp. 129-146.

(4) Lynn, Randall S., Wong, Kien K., Clark, Hector Mel, 1991, "On the Particle Size Effect in Slurry Erosion," Wear, Vol. 149, pp. 55-71.

(5) Clark, Hector McI, 1993, "Specimen Diameter, Impact Velocity, Erosion Rate and Particle Density in a Slurry Pot Erosion Tester," Wear, Vol. 162-164, pp. 669-678.

(6) Clark, Hector McI., Wong, Kien K., 1995, "Impact Angle, Particle Energy and Mass Loss in Erosion by Dilute Slurries," Wear, Vol. 186-187, pp. 454-464.

(7) Stack, M. M., Pungwiwat, N., 1999, "Slurry Erosion of Metallics, Polymers, and Ceramics: Particle Size Effects," Materials Science and Technology, Vol. 15, pp. 337-344.

(8) Turenne, S., Fiset, M., Masounave, J., 1989, "The Effect of Sand Concentration on the Erosion of Materials by a Slurry Jet," Wear, Vol. 133, pp. 95-106.

(9) Wheeler, D. W., Wood, R. J. K., 1999, "Solid Particle Erosion of CVD Diamond Coatings," Wear, Vol. 233-235, pp. 306-318.

(10) Ninham, A. J., Levy, A. V., 1988, "The Erosion of Carbide-Metal Composites," Wear, Vol. 121, pp. 347-361.

(11) Ball, A., Willmott, S., Resente, A., 1988, "The Erosion of Candidate Materials for Valves in Coal Gasification Systems," Wear, Vol. 123, pp. 225-239.

(12) Humphrey, J. A. C., 1990, "Fundamentals of Fluid Motion in Erosion by Solid Particle Impact," Int. J. Heat and Fluid Flow, Vol. 11, No. 3, pp. 170-195